Texas A&M University
Mechanical Engineering Department
Turbomachinery Laboratory
Tribology Group

Effect of Side Feed Pressurization on the Performance of Shimmed Foil Gas Bearings – Part I: Experimental Verification

by

Tae Ho Kim
Research Assistant

Luis San Andrés
Mast-Childs Professor
Principal Investigator

May 11, 2007

EXECUTIVE SUMMARY

The report presents measurements of the rotordynamic performance of a rigid rotor supported on Gas Foil Bearings (GFBs). In high temperature applications, GFBs often require of adequate thermal management. Pressurized gas feed through one of the GFB ends forces a cooling stream to carry away thermal energy from a hot turbine, for example. Incidentally, side gas pressurization in GFBs has shown a paramount effect in reducing rotor amplitudes of motion.

2006 TRC report shows, for the rotor-GFB system tested to a speed 25 krpm, a linear synchronous response behavior for moderately small imbalances and while operating with a low feed gas pressure of 0.34 bar (5 psig). At higher rotor speeds, reaching to 50 krpm, subsynchronous whirl motions reach limit cycles of large amplitude and associated to low natural frequency rigid body modes. Presently, further rotordynamic response measurements are conducted during rotor speed-up and coastdown tests for GFBs supplied with increasing feed pressures to 4.1 bar (60 psig). The tests show the dramatic effect of bearing side gas pressurization on reducing the total amplitude of rotor motion, mainly composed of one subsynchronous whirl frequency. At a given rotor speed and for sufficiently high feed pressure into the GFBs, the rotor subsynchronous whirl motions disappear; i.e. the test system becomes rotordynamically stable. With a side feed pressure of 0.34 bar (5 psig), speed coastdown rotor responses from 25 krpm and for large imbalances demonstrate a nonlinear effect with an evident reduction in system damping. In general, side gas pressurization has little effect on ameliorating the amplitudes of rotor synchronous response.

Installation of metal shims under the GFB bump strip layers and in contact with the bearing cartridge introduces a mechanical preload into the test bearings. The preload makes the bearings stiffer and aids to increase the system threshold speed of instability. At high shaft speeds, however, subsynchronous motions become dominant, and whose amplitudes are aggravated by increasing rotor imbalance. A feed gas pressure of 4.1 bar (60 psig) delays significantly the threshold speed of subsynchronous motions. For small imbalances, normalization of the amplitudes of synchronous motion demonstrates the test system linearity. Recorded loci of rotor static centerline show that side gas pressurization reduces cross-coupled force effects that destabilize the rotor-GFB system at high rotational speeds.

The comprehensive measurements validate computational predictions advanced in a companion report. The experimental program furthers the application of GFBs into oil-free micro-turbomachinery.

TABLE OF CONTENTS

LIST OF TABLES

LIST OF FIGURES

NOMENCLATURE

C_{eff}	Effective damping coefficient[N·s/m]
c_{DE} , c_{FE}	Nominal radial clearance for the drive and free end GFBs, respectively [m]
c_J	Journal radial travel [m]
DV, DH	Drive end bearing, vertical and horizontal planes
FV, FH	Free end bearing, vertical and horizontal planes
g	Gravity
K_{eff}	Effective stiffness coefficient [N/m]
M	Fraction of the rotor mass that each bearing supports [kg]
m_e	Mass imbalance [mg]
N_{os}	Onset speed of subsynchronous rotor motions [rpm]
r	Radius for location of imbalance masses [m]
u	m_e *r/M,* Imbalance displacement [μm]
X, Y	Vertical and horizontal rotor displacements
WFR	Whirl frequency ratio [-]
ξ	Damping ratio [-]
Ω	Rotor angular speed [rad/s]
ω_{cr}	Critical speed [rad/s]
ω_n	Natural frequency of the rotor-GFB system [rad/s]

Subscripts

DE,FE	Rotor drive and free end, respectively.

I. INTRODUCTION

Implementing gas foil bearings (GFBs) in micro turbomachinery reduces system complexity and maintenance costs, and increases efficiency and operating life [1]. Bump type GFBs comprise of one or more arcuate top foils supported by elastic support layers. The compliant underlying structure provides structural stiffness and damping arising from material hysteresis and dry-friction [2,3]. GFBs have larger film thickness than rigid gas bearings, thus improving operational reliability and providing a solution for problems related to the thermal expansion of both a journal and its bearing [4]. GFBs with engineered solid lubricants (coatings) are being developed for application in high temperature environments [5]. Adequate thermal management for operation in high temperature environments is an issue of importance in applications such as in gas turbines and turbochargers [6].

In addition to heat conduction through the support structure consisting of the top foil and elastic support layers, GFBs often need a cooling gas flow, axially fed through one end of the bearing, to transport the heat conducted from a hot turbine, for example [7]. Introducing the cooling flow prevents hot-spots in the GFB and extends its life. Side gas pressurization, however, shows a paramount effect on reducing amplitudes of motion, synchronous and subsynchronous [8].

Introducing mechanical preloads into GFBs enhances the hydrodynamic wedge to generate a pressure field producing a centering stiffness even in the absence of an applied static load [9]. Mechanical preloads can be given to GFBs with a differential height of the elastic support, by introducing "lobe" shape inner profile of the machined GFB bore, or by performing the top foil and elastic support layers to have larger radius of curvature than that of the GFB bore [9-10]. However, the easiest and most cost effective way is by inserting metal shims underneath a bump strip and in contact with the bearing housing [9].

This report describes experimental results of the rotordynamic performance of a rotor supported on two GFBs with side pressurization. Installation of three metal shims into GFBs reveals the effect of mechanical preload on the dynamic performance. A series of rotor speed-up tests to 50 krpm identify the onset speeds of subsynchronous motion for GFBs with side feed pressurization. Phase angle and amplitude of synchronous rotor responses for increasing in-phase and out-of-phase imbalance masses are recorded during coastdown tests. Normalization of the rotor amplitudes after baseline subtraction aids to evaluate the linearity of the rotor – GFB

system. A single degree of freedom model estimates the effective stiffness and damping ratio from the measured rotor responses. Rotor speed versus time data obtained during rotor coastdown tests serves to identify speed ranges where "viscous" drag is dominant.

II. LITERATURE REVIEW

In 1953 Block and van Rossum [4] introduced the concept of Foil Bearings (FBs). The authors point out that a foil bearing film thickness, larger than that of rigid gas bearings, can improve operational reliability and provide a solution for problems related to thermal expansion of both a journal and its bearing. Field experience has proved, since the late 1960's, that Gas Foil Bearings (GFBs) are far more reliable than ball bearings previously used in Air Cycle Machines (ACMs) installed in aircrafts. Therefore, GFBs have since been used in almost every new ACM installed in both civil and military aircraft [1]. Implementation of GFBs into high performance turbomachinery applications demands accuracy in modeling capabilities. Engineered GFBs must have a dimensionless load capacity larger than unity, i.e., specific pressure (W/LD) > p_a [11].

Ruscitto et al. [12] perform a series of load capacity tests of "first generation" bump type foil bearings [5]. The test bearing, 38 mm in diameter and 38 mm in length, has a single top foil and a single bump strip layer. The authors note that the actual bearing clearance for the test bearing is unknown. Thus, the journal radial travel (c_J) was estimated by performing a static load-bump deflection test. The authors installed displacement sensors inside the rotor and measure the gap between the rotor and the top foil at the bearing's center plane and near the bearing edge. As the static load increases, for a fixed rotational speed, the minimum film thickness and journal attitude angle decrease exponentially. The test data for film thickness is the only one available in the open literature.

Heshmat [13] introduces single foil, multistage bump strip layers to engineer tunable bearing support stiffness along the radial and circumferential directions. The designed stiffness gradient ensures a hydrodynamic wedge or a lobe-like effect for enhanced generation of hydrodynamic pressure. As the shaft speed increases, gas pressure pushes the top foil and bumps outwards, thus forming a converging wedge film shape. In the experiments, a multistage bump strips GFB, 35 mm in diameter and 31 mm in length, achieves an impressive ultimate load capacity of 728 N [6.73 bar (98 psi) specific pressure]. Heshmat also demonstrates the successful operation of GFBs to a maximum speed of 132 krpm, i.e. 4.61×10^6 DN value; albeit the vibration

2

measurements show large amplitude subsynchronous whirl motions related to the test rotor rigid body mode natural frequencies. However, in spite of the subsynchronous whirl, the rotor reached a stable limit cycle operation.

Chen et al. [9] replace a tape-type foil bearing with a bump-type foil bearing in a helium turbocompressor. The paper describes the design and fabrication of a bump-type foil bearing, and presents a comparison in rotordynamic performance tests for the original tape-type foil bearings and the replacement bearings. The bump-type foil bearings have one top foil supported on three bump strip layers. To enhance the dynamic stability of a compressor rotor operating in the vertical direction, a shim was installed at the middle of each bump layer, thus providing a radial preload to the foil bearings. The frictional torque of the foil bearings is significant before rotor lift-off and decreases once the rotor speed is high enough to generate a hydrodynamic film pressure. Steady state and speed transient tests show that the implementation of the bump-type foil bearing increased the critical speed of the original system because the bearing stiffness is greater than that of the original rotor supported on tape-type bearings.

Bauman [7] introduces a thrust GFB test rig for use in future oil-free gas turbines being developed at NASA. The test rotor supported on a thrust GFB and two journal GFBs operates to a top speed of 80,000 rpm and temperatures up to 650 ºC (1200 ºF). A hydrostatic loader piston provides an axial load to the shaft, and a magnetic thrust bearing counteracts the test thrust GFB loads ensuring a steady motion of the thrust runner. Cooling air is supplied into the test rig housing to carry away waste heat from the magnetic thrust bearing as well as the heat conducted from a hot turbine to the journal GFB. The axially fed cooling flow prevents hot-spots in the GFB and extends its life. Measurement parameters of the test rig include bearing torque, load capacity, and bearing temperature, which will be used to validate computational models of GFBs.

Lubell et al. [6] evaluate high temperature coatings for GFBs used in oil-free micro gas turbine engines. The solid lubricant not only reduces friction torque during the start-up and shut-down of turbomachinery supported on GFBs, but also prevents failures related to coating degradation of the shaft and bearings at high temperatures, well above 500 ºC (930 ºF). The paper describes a micro gas turbine engine test with a shaft coated using PS304 developed by NASA. The shaft is supported on a GFB in the hot section. During endurance engine tests, two coating related failures were recorded. Subsequently, new coating procedures were adopted, i.e. plasma spray on the shaft with an oblique angle at both shaft end locations and simple heat

treatment of coated parts prior to final surface grinding. These procedures coat the shaft surface uniformly and enhance the coating adherence, thus improving the coating micro-structural stability characteristics at high temperature operation. Further engine tests demonstrated successful operation at 500°C (930°F) for over 2,500 hours and 2,900 start-stop cycles without damage or loss of performance.

Recently, San Andrés et al. [8] investigate the rotordynamic performance of a rotor supported on GFBs. A series of coastdown tests with small to large imbalance masses inserted in a hollow rotor demonstrate that large imbalance masses induce subsynchronous motions of large amplitude and associated with low frequency rigid body modes. Rotordynamic model predictions do not correlate well with the test data. A comparison of normalized imbalance response amplitudes reveals a nonlinear rotor behavior since the GFB stiffness and damping coefficients are apparently amplitude and frequency dependent. External air pressurization through the bearing ends aids to reduce the amplitude of synchronous motions while crossing a critical speed. Incidentally, the tests also demonstrate that increasing air pressurization ameliorates the amplitudes of subsynchronous motions due to the significant effect of the axial flow retarding the circumferential flow development within the gas bearings.

San Andrés and Kim and [14] enhance the computational model developed in [15] to predict the performance of GFBs with mechanical preloads. In Ref. [15], the FE model considers the top foil as a structural shell and integrates it with the bump strip layers in conjunction with the hydrodynamic gas film to predict the static and dynamic load performance of GFBs. Installation of three metal shims underneath a bump strip and in contact with the bearing housing provides mechanical preloads to the test GFB. The location, length, and thickness of the shims determine the inner profile of the bearing compliant surface, similar to the configuration of a "three lobe bearing". The model predictions in [14] show a hydrodynamic pressure development even without a static load, i.e., centered rotor operation, and reveal that the preloads do not affect the load capacity, but increase the direct stiffness and damping coefficients, thus enhancing the stability characteristics of GFBs.

III. EXPERIMENTAL PROCEDURE

Rotordynamic response measurements for increasing imbalance masses are conducted on a rotor supported on GFBs. The bearings are air pressurized at one end only; the other end is exposed to ambient pressure. A 2006 TRC report [16] details the geometry and materials of the test rotor and second generation GFBs. Briefly, the rotor weighs 1 kg, and the GFB length L and shaft diameter ($2R_J$) are 38.1 mm, with estimated sway radial clearances of $c = 40$ and 70 um for the drive and free end GFBs, respectively. Figure 1 shows the GFB test rig for the rotordynamic experiments [16]. The test rig housing holds two test GFBs and contains an internal duct to supply air pressure up to 7 bars (100 psig) for cooling the bearings, if needed. The air pressurization at rotor midspan forces a cooling flow through the test GFBs. A 0.75 kW (1 HP) AC electric motor with maximum speed of 50 krpm drives the test rotor through a flexible coupling. A router AC motor, 1.49 kW (2.0 HP) with maximum speed of 25 krpm, aids the driving motor to start up the test rotor through a centrifugal clutch before the rotor lifts off from its bearings. See Ref. [16] for a more detailed description of the test rig and bearings.
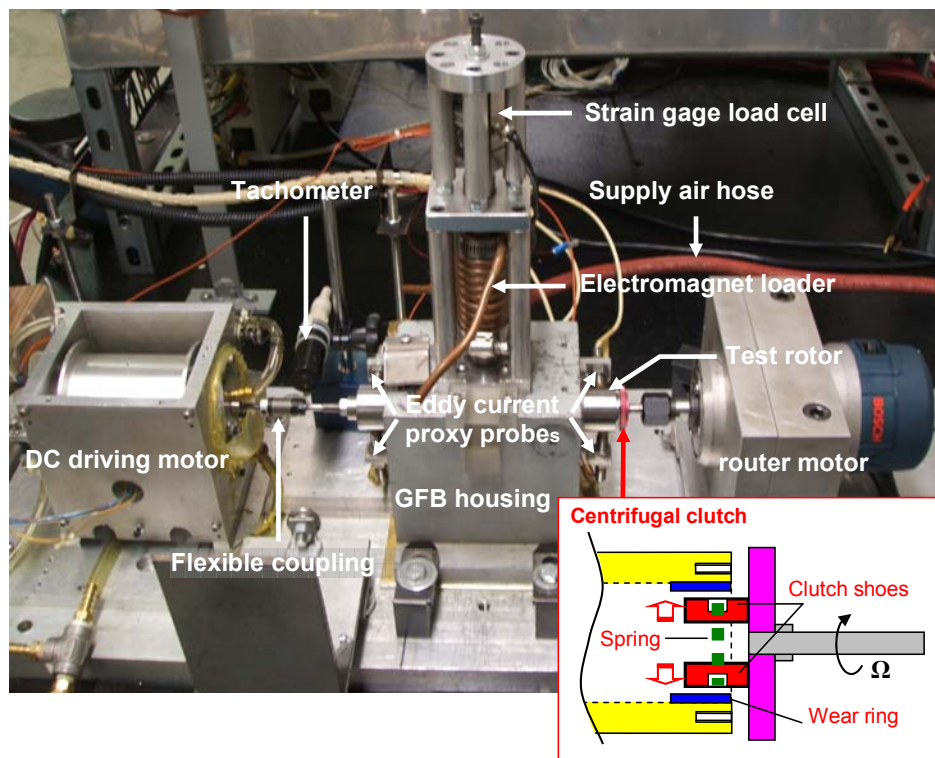
Figure 1. Test rig for rotordynamic tests of a rotor supported on GFBs [16]

Tests are conducted at ambient temperature, $T = 293º$ K. Ref. [16] shows severe subsynchronous rotor motions above 26 krpm at a side pressure of 0.35 bar (5 psig). The large amplitude whirl motions reach limit cycles with frequencies coinciding with the low natural frequency rigid body modes of the rotor bearing system. At rotor speeds lower than 26 krpm, no subsynchronous motions are observed. Normalized synchronous amplitudes show a linear rotor response behavior when using moderately small imbalance masses of 55 mg, 110 mg, and 165 mg. These results are in opposition to those in [8]; increasing normalized synchronous amplitudes with increasing imbalance masses. Note that only a well balanced rotor in [16] ensures a linear rotor behavior.

Presently, further imbalance response measurements are conducted at a side pressure of 0.35 bar (5 psi) for in-phase and out-of-phase large imbalance mass of 330 mg, i.e. six times the lowest imbalance mass of 55 mg. Normalized rotor amplitudes and phase angles of the measured synchronous responses with the large imbalance mass are compared to those with small to moderate imbalance masses in [16]. A one degree of freedom mechanical system model aides to identify the natural frequency, effective stiffness, and damping ratio of the test GFBs.

Table 1 shows the imbalance masses added into the rotor end planes at radius (r) equal to 15.11 mm. The table includes the masses angular disposition (in-phase and out-of-phase) as well as the equivalent imbalance displacements (u).

Table 1 Imbalance masses, equivalent imbalance displacements, and their location at rotor end planes

Imbalance test type		Imbalance mass (m_e)		Imbalance displacement (u)	
		Drive end	Free end	Drive end	Free end
In-phase	Test 1	55 mg (-45º)	55 mg (-45º)	1.26 µm	2.34 µm
	Test 2	110 mg (-45º)	110 mg (-45º)	2.52 µm	4.67 µm
	Test 3	165 mg (-45º)	165 mg (-45º)	3.78 µm	14.0 µm
	Test 4	330 mg (-45º)	330 mg (-45º)	7.56 µm	7.56 µm
Out-of-phase	Test 1	55 mg (-45º)	55 mg (135º)	1.26 µm	2.34 µm
	Test 2	110 mg (-45º)	110 mg (135º)	2.52 µm	4.67 µm
	Test 3	165 mg (-45º)	165 mg (135º)	3.78 µm	7.00 µm
	Test 4	330 mg (-45º)	330 mg (-45º)	7.56 µm	14.0 µm

Imbalance displacement, $u_i = m_e \times r / M_{i, \ i=DE, FE}$.
The masses (M_{DE}, M_{FE}) represent a fraction of the rotor weight (divided by gravity) acting on each bearing: 0.66 kg and 0.36 kg for drive end and free end bearings, respectively. The coupling force is not considered for the static load distribution.

Rotor speed-up tests are also conducted on the same rotor supported on side pressurized GFBs for small to moderate imbalance masses of 55 mg, 110 mg, and 165 mg. The bearings are air pressurized at one end only; the other end is exposed to ambient pressure. The air supply pressure level is controlled manually.

Processing of the test data reveals the onset rotor speeds of subsynchronous whirl motions for increasing side pressures of 0.35 bar (5 psig), 1.4 bar (20 psig), and 2.8 bar (40 psig). Rotor speed coastdown tests from 25 krpm[1] are conducted for increasing side feed pressures. A comparison of the recorded synchronous rotor motions reveals the effect of side pressurization on the natural frequency and damping ratio of the rotor-GFB system.

Three metal shims of 25.4 μm thickness, 8.6 mm width, and 38.1 mm length are installed under the bump strip and in contact with the bearing housing at three angular locations. Figure 2 shows the schematic views of the original test GFB and the modified GFB with three shims. The original test GFB consists of five arcuate bump strips, each with five bumps. The end of a bump strip is welded to the bearing sleeve while the other end is free. The top foil, coated with a spray-on Teflon® type coating of thickness 25.4 μm, consists of a thin metal sheet welded at the bearing sleeve at one end (spot weld) and free at the other end. Figure 2 notes the orientation of the top foil spot-weld with respect to the vertical (gravity) plane is noted. Table 2 lists the geometry and material properties of the test GFB with shims. Each shim has an angular extension of 26 º, and the arc distance between adjacent shims is 120 º.

A rotor speed-up (acceleration) test determines the threshold speed of instability where subsynchronous motions suddenly begin to increase. The side feed pressure is manually increased from 0.35 bar (5 psig) to 4.1 bar (60 psig) during the rotor speed-up tests to 50 krpm. Imbalance rotor responses are measured during coastdown tests from 35 krpm[2] for in-phase and out-of-phase imbalance masses of 55 mg and 110 mg. Normalization of the synchronous rotor amplitudes aids to verify the linearity of the system response within the speed range of 0 to 35 krpm. The measured synchronous and subsynchronous rotor motions for increasing side feed pressures are analyzed. In addition, the estimated loci of static rotor centerline are compared for tests with increasing side feed gas pressure into the bearings.

---

[1] Onset speed of subsynchronous rotor motions for a side pressure of 0.35 bar supplied to the original GFBs.
[2] Onset speed of large subsynchronous rotor motions for air pressure of 0.35 bar supplied to the test GFBs with shims.
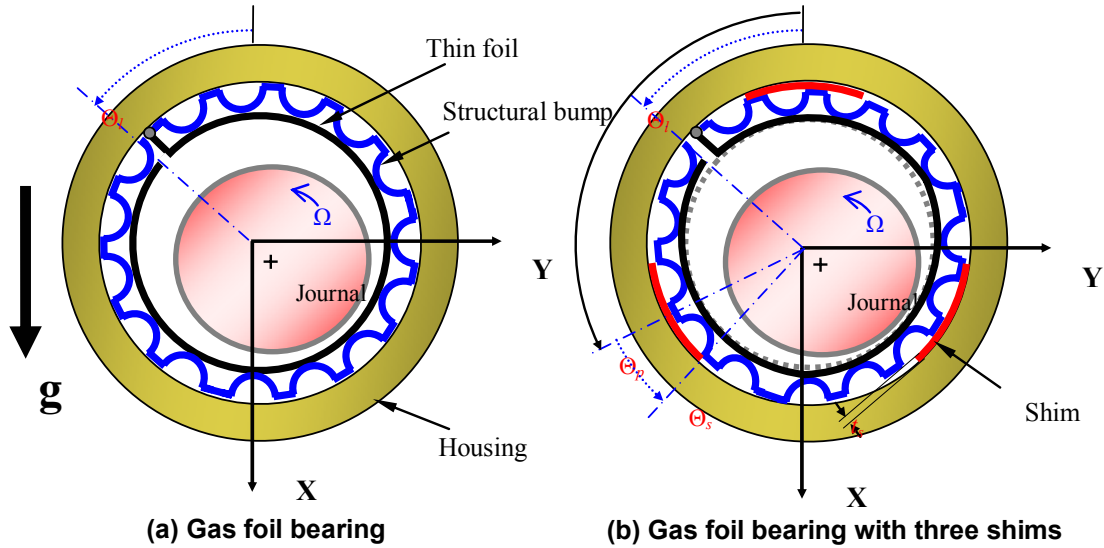
Figure 2. Schematic views of original test GFB and modified GFB with three metal shims. Locations of top foil leading edge and shims relative to vertical plane as in tests.

Table 2 Geometry of modified GFB with shims

Bearing	Radius, $R=D/2$	19.05 mm	(0.75 inch)
	Length, L	38.1 mm	(1.5 inch)
	Top foil arc circumferential length, l_x	120 mm	(4.7 inch)
	Angular distance between top foil leading edge and vertical plane, Θ_l	45 °	
Shims	Angular distance between adjacent shims, Θ_p	120 °	
	Axial length, L_s	38.1 mm	(1.5 inch)
	Thickness, t_s	25.4 μm	(1.0 mil)
	Width, w_s	8.6 mm	(0.34 inch)
	Angular extent, Θ_s	26 °	
	Number, N_s	3	
	Material	Steel	
Bump	Pitch, p	4.572 mm	(0.18 inch)
	Length, l_o	4.064 mm	(0.16 inch)
	Foil thickness, t	0.102 mm	(4.0 mil)
	Height, h	0.381 mm	(15 mil)
	Poisson's ratio, υ	0.29	
	Bump modulus of elasticity, E	213 GPa	(30.9 Mpsi)
	Dry friction coefficient, μ (estimated)	0 - 0.25 [17]	

IV. MEASUREMENTS OF ROTOR MOTION IN TEST ROTOR-GFB SYSTEM: ORIGINAL GFBS CONFIGURATION

IV-1. Onset speed of subsynchronous motions (rotor speed-up tests)

A rotor speed-up (acceleration) test identifies the onset speeds of subsynchronous rotor motion for increasing side pressures. The rotor speed is manually controlled to accelerate the rotor from the minimum motor control speed (10 krpm) to rotor speeds well above the onset speeds. Figures 3 (a) and (b) display waterfall plots of vertical motions recorded at the rotor free end for side gauge pressures of 0.35 bar (5 psig) and 2.8 bar (40 psig), respectively. Subsynchronous motions of large amplitude are evident as the rotor speed increases. Figure 4 depicts the amplitudes of rotor synchronous and subsynchronous motions recorded at the rotor free end for side feed pressures of 0.35 bar (5 psig), 1.4 bar (20 psig), and 2.8 bar (40 psig). With a low feed pressure of 0.35 bar, the onset speed of subsynchronous motion (N_{os}) is 25 krpm. This rotor onset speed increases to 30.5 krpm as the side gauge pressure is raised to 2.8 bar.

As vividly shown in Figure 5, FFT spectra of shaft motions at a shaft speed of 30 krpm (500 Hz), the severity of subsynchronous amplitudes is directly related to the amount of side pressurization. The frequency of subsynchronous whirl corresponds with a rigid body natural frequency the rotor-GFBs system. This natural frequency changes little with the magnitude of side feed pressurization. Figure 6 shows the dramatic effect of side gas pressurization on reducing the total amplitude of motion, mainly composed of the subsynchronous whirl motions. For $P_s \geq 2.8$ bar the rotor subsynchronous whirl motions disappear; i.e. the test system is rotordynamically stable at 30 krpm.
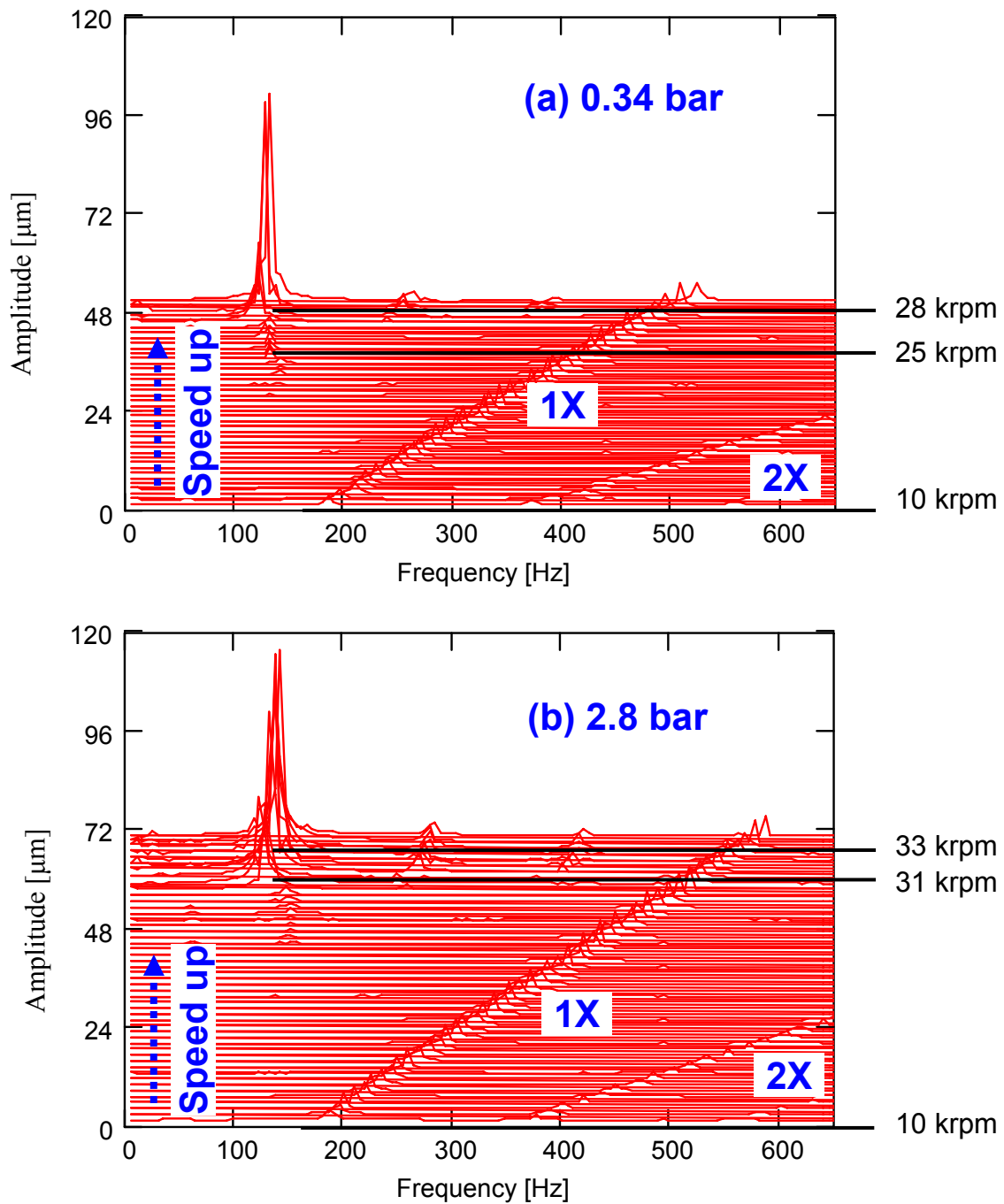
Figure 3. Waterfall of rotor speed-up response from 10 krpm. Baseline imbalance condition, feed air gauge pressures (a) 0.34 bar (5 psig) and (b) 2.8 bar (40 psig). Vertical displacements recorded at rotor free end. Original GFBs.
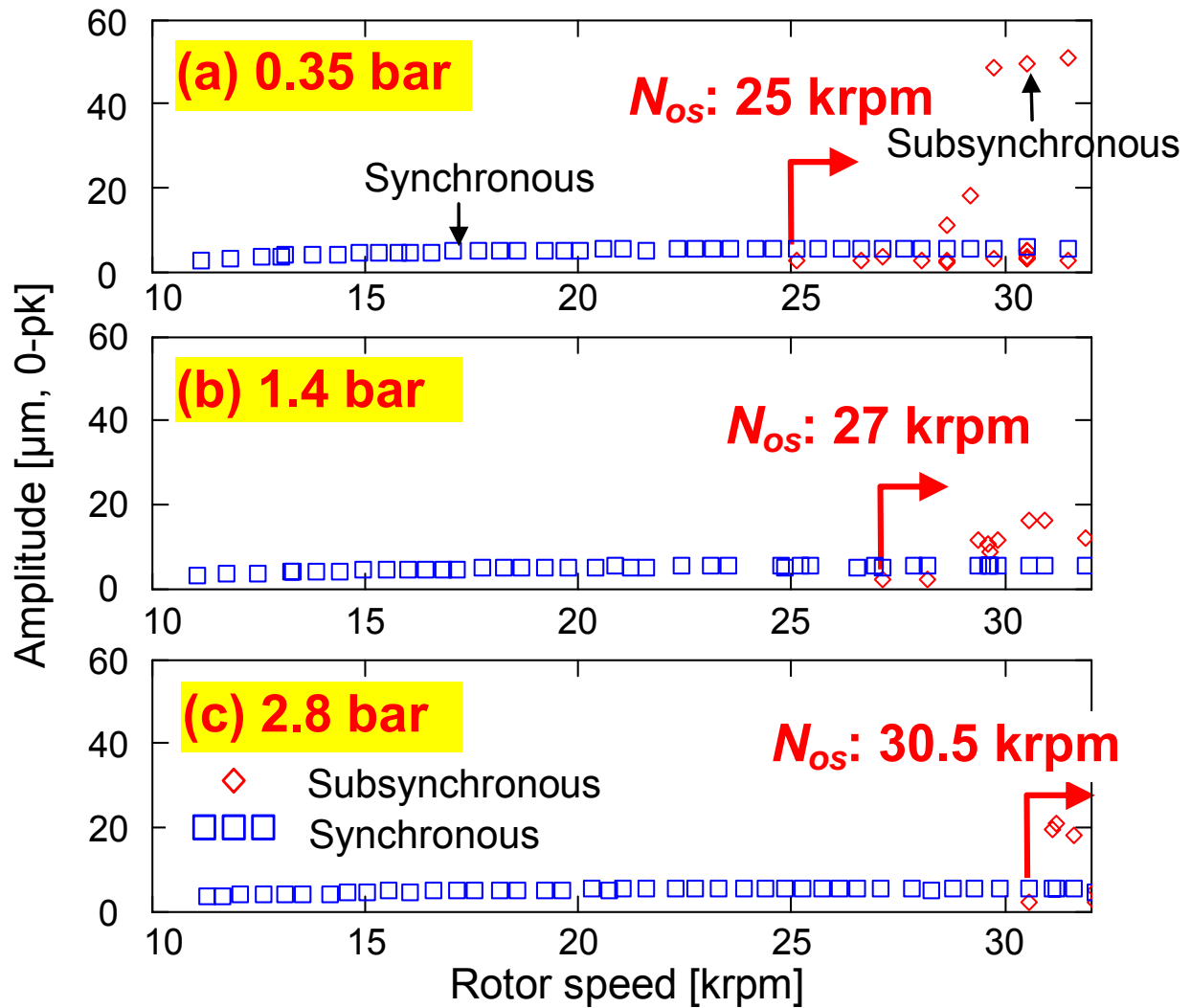
Figure 4. Amplitudes of synchronous and subsynchronous rotor motions for increasing feed side gauge pressures versus shaft speed. Vertical displacements (*X*-direction) at rotor free end. Rotor half mass: 0.5 kg. N_{os}: onset speed of subsynchronous motions. Original GFBs.
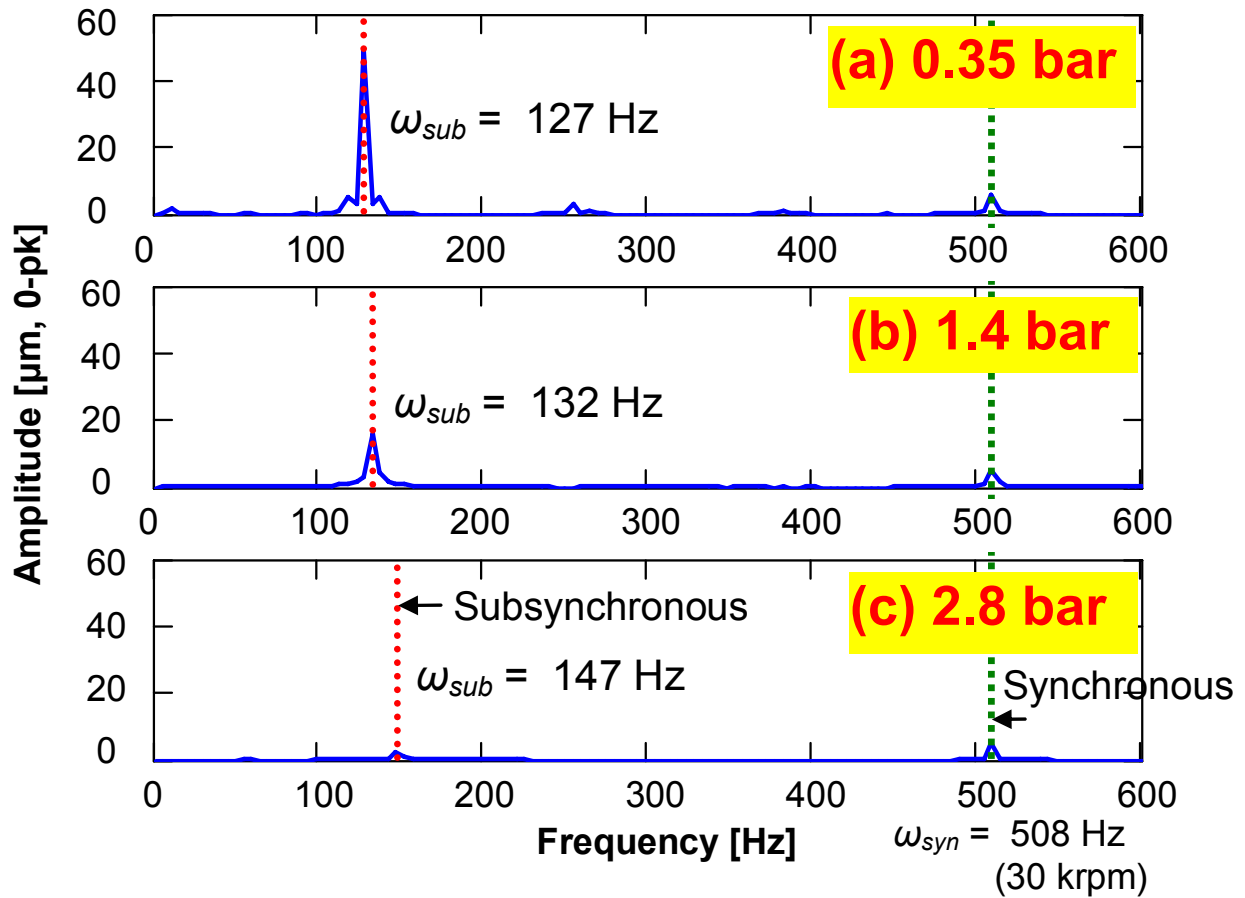
Figure 5. Spectra of rotor motions for increasing feed (gauge) side pressures and operation at 30 krpm (500 Hz). Original GFBs.
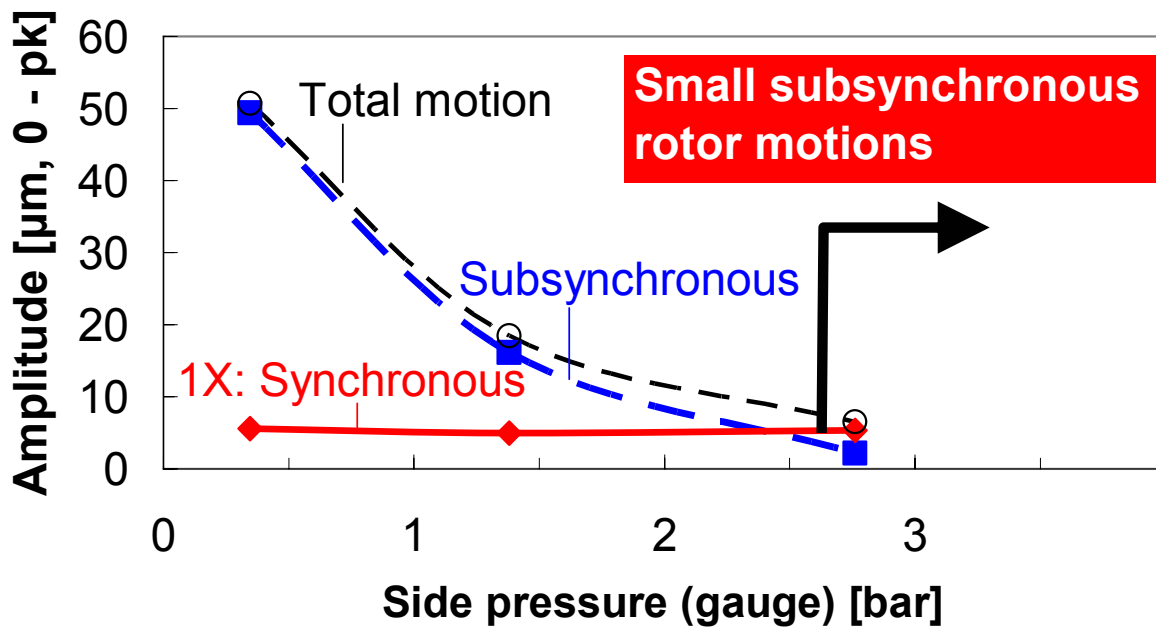
Figure 6. Amplitudes of total shaft motion, and synchronous and subsynchronous components versus side gas pressurization at 30 krpm (500 Hz). Original GFBs.

IV-2. Synchronous response amplitude and phase angle (rotor coastdown tests)

Imbalance response measurements are conducted during rotor coastdown test from 25 krpm at a side gauge pressure of 0.35 bar (5 psig) for in-phase and out-of-phase large imbalance mass of 330 mg, i.e. six times the minimum imbalance mass of 55 mg (imbalance distances, u=1.3 μm and 2.3 μm, for the rotor drive and free ends). Figures 7a and 7b show the normalized rotor amplitudes and phase angles of the measured synchronous responses with the large imbalance mass, and compare them to those with small to moderate imbalance masses reported in [16]. The recorded imbalance responses are subtracted using a baseline response (amplitude and phase) and normalized by multiplying the response by the ratio of the smallest imbalance divided by the actual imbalance [16]. The figures display the vertical motions at the rotor drive end. Each phase angle is shifted an offset to discard the influence of an imbalance mass angular disposition on the recorded data (e.g., a shifted offset of -45 º at the drive end, vertical plane for both in-phase and out-of-phase imbalance conditions).

For the smallest to moderate imbalance masses, the test data evidence nearly uniform normalized amplitudes and phase angles, i.e., characteristic of a linear system. On the other hand, with a large imbalance mass of 330 mg, the peak amplitude around the critical speed (ω_{cr}) increases significantly, in particular, for the out-of-phase imbalance test. The critical speed of the rotor-bearing system decreases by ~3 krpm when compared to those estimated with the smallest to moderate imbalance masses. The phase angle of ~ 90 º determines similar natural frequency for all imbalance conditions. With the large imbalance mass, the phase angle increases more rapidly around the natural frequency, showing a reduction in equivalent viscous damping. Thus, a large imbalance mass causes a nonlinear response of the rotor – GFB system as discussed in [8]. Note, however, that the added imbalance mass appears not to change the system natural frequency, i.e. the system effective stiffness appears indifferent to the magnitude of added imbalance mass.

Note that, in Figs. 7a and 7b, a large imbalance mass of 330 mg results in different trends of phase angles from those with small to moderate imbalance masses; the phase angle is not toward 180 º as the rotor speed increases. This may be caused due to a lack of viscous damping with the large imbalance mass; for example, in a dry-friction damping model, the phase angle is independent of the frequency of a response[3] [18].

Appendix A shows the normalized amplitude and phase angle of the rotor synchronous response for the free end bearing, vertical plane. Appendix B shows the determination of the effective stiffness (K_{eff}), damping ratio (ξ), and effective damping (C_{eff}) derived from the rotor responses to moderate and large imbalance masses.

---

[3] Ginsberg [18] also notices that a large amplitude dynamic force (F), a small dry-friction coefficient (μ), and a small normal load (N) lead to null energy dissipation (a typical result from the dry-friction effect for operation of the system) at the natural frequency, thus causing significantly large amplitude peaks at this frequency, i.e. E_{diss} =0 if $\mu N/F < \pi/4$. Therefore, it is readily inferred that a small imbalance mass, a heavy rotor mass, and a large dry-friction coefficient aid to reduce rotor amplitude peak at the natural frequency of the rotor-GFB system.
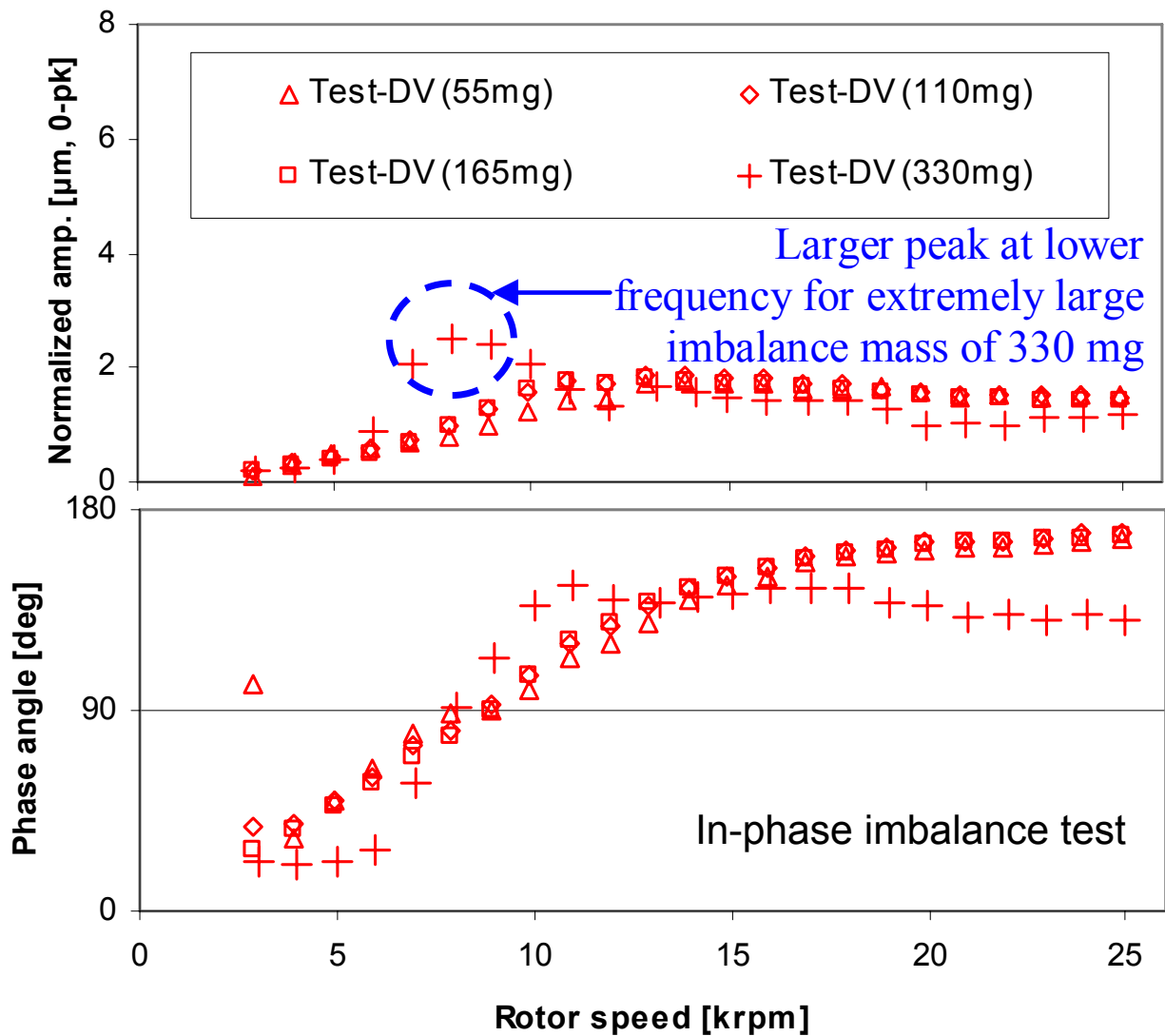
Figure 7a. Influence of large imbalance mass on normalized amplitude and phase angle of synchronous response. In-phase imbalance masses of 55mg, 110mg, 165mg, and 330mg. Measurement at drive end bearing, vertical plane with baseline subtraction. Side feed gauge pressure at 0.34 bar (5 psig). Original GFBs.
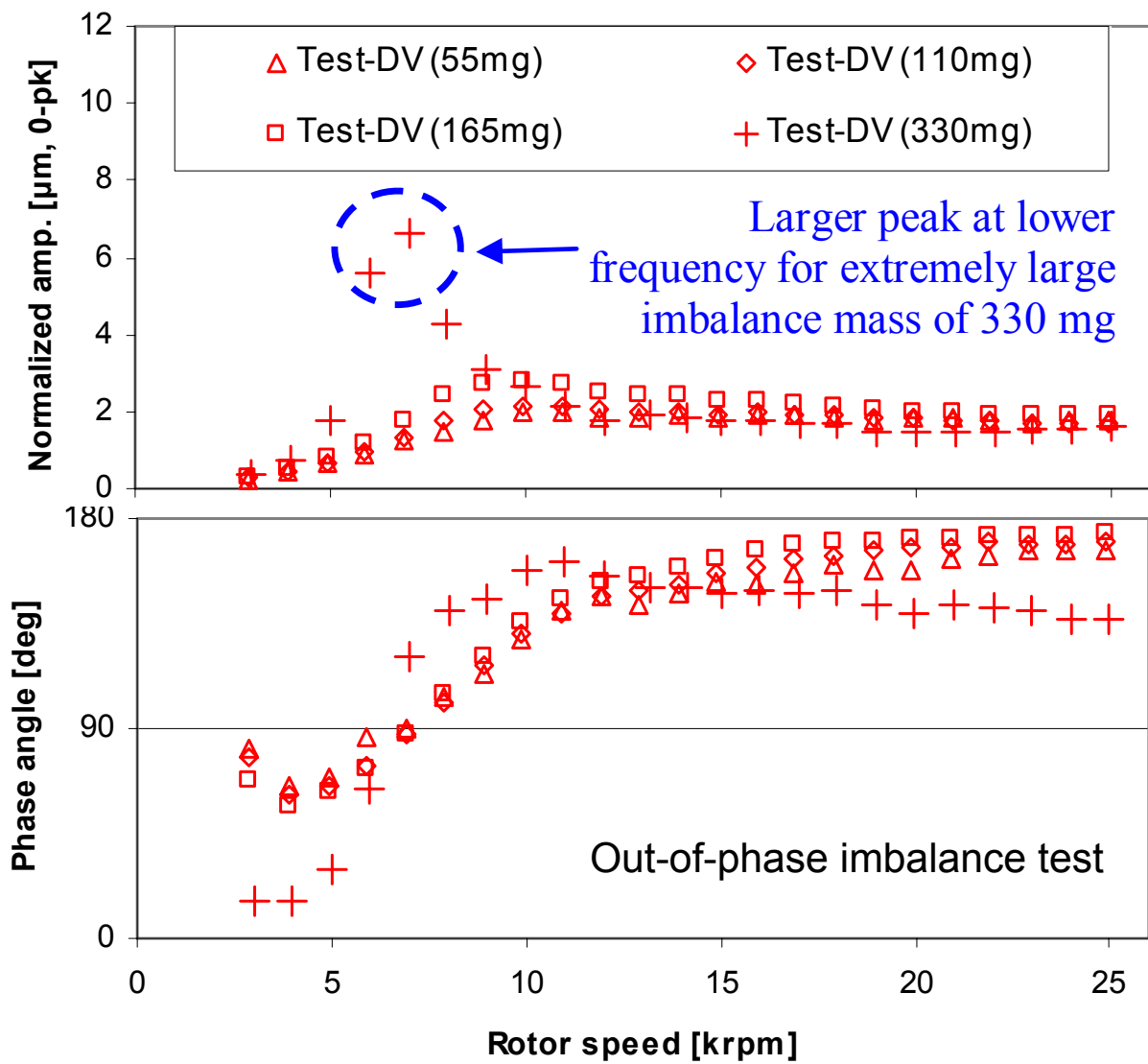
Figure 7b. Influence of large imbalance mass on normalized amplitude and phase angle of synchronous response. Out-of-phase imbalance test responses with imbalance masses of 55mg, 110mg, 165mg, and 330mg. Measurement at drive end bearing, vertical plane with baseline subtraction. Side feed gauge pressure at 0.34 bar (5 psig). Original GFBs.

Note that the large imbalance mass of 330 mg causes subsynchronous rotor motions of large amplitude at rotor speeds as low as 18krpm. Figures 8a and 8b show coastdown rotor responses for large and small imbalance masses of 330 mg and 55 mg, respectively. For the large added imbalance (330 mg), the rotor shows whirl frequency ratios (*WFR*=subsynchronous whirl frequency / rotor speed) equal to 0.33 (1/3 *X*) and 0.66 (2/3*X*) from 28 krpm to 18 krpm; while for the small imbalance mass (55 mg) the rotor shows *WFR*s equal to 0.25 (1/4*X*) and 0.5 (1/2*X*) from 35 krpm to 27 krpm. Note, however, that for the small imbalance mass (55 mg), the recorded relatively small amplitudes of subsynchronous rotor motions appearing between 23 krpm and 30 krpm show a *WFR* equal to 0.33 (1/3*X*).
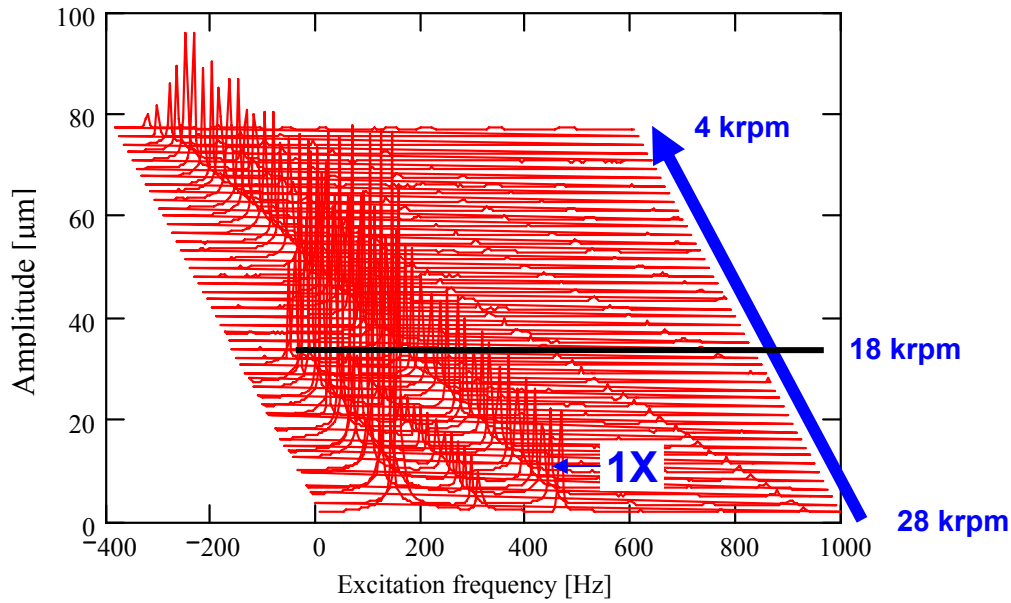
(a) Waterfall
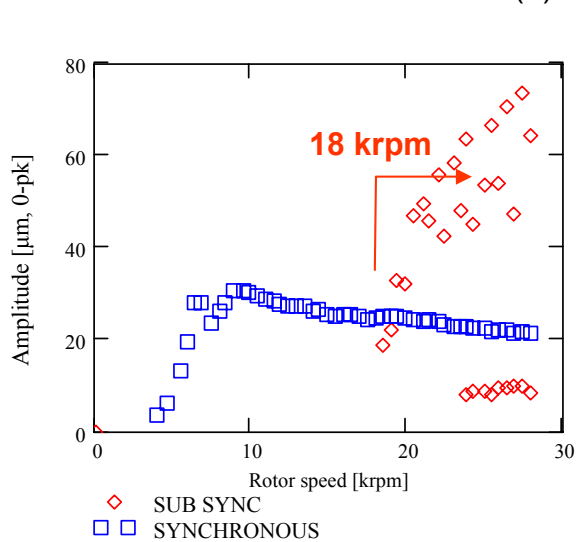
(b) Synchronous and subsynchronous components
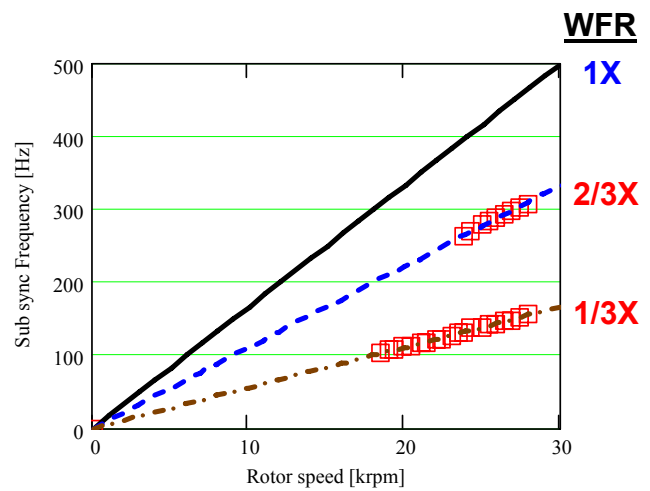
(c) Subsynchronous whirl frequency

Figure 8a. Coastdown rotor response from 28 krpm. Out-of-phase imbalance mass of 330 mg, side air gauge pressure of 0.34 bar (5 psig). Measurement at rotor free end, vertical plane. Original GFBs.

(a) Waterfall
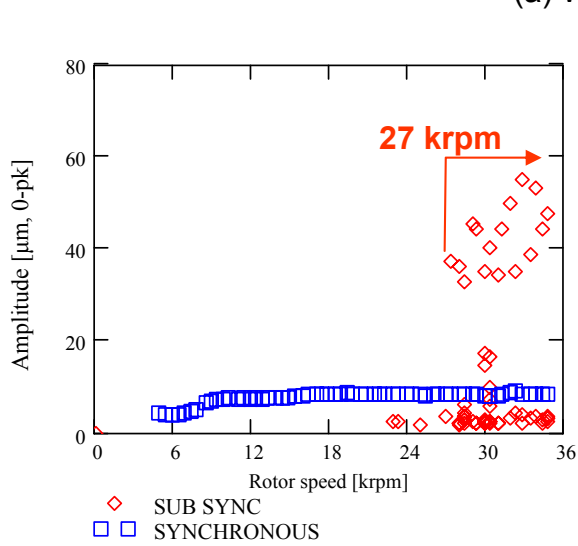
(b) Synchronous and subsynchronous components

(c) Subsynchronous whirl frequency

Figure 8b. Coastdown rotor response from 35 krpm. Out-of-phase imbalance mass of 55 mg, side air gauge pressure of 0.34 bar (5 psig). Measurement at rotor free end, vertical plane. Original GFBs.

Further imbalance response measurements are conducted on GFBs with side pressurization for small to moderate imbalance masses of 55 mg, 110 mg, and 165 mg. At increasing side feed pressures of 1.4 bar (20 psig) and 2.8 bar (40 psig), test results present nearly uniform normalized amplitudes and phase angles, i.e., characteristic of a linear system and similar to those for 0.34 bar (5 psig) feed pressure as shown in Fig. 7 (See also Appendix C).

The normalized rotor amplitudes and phase angles for the increasing imbalance masses at each side pressure are arithmetically averaged, for a comparison to the averaged results at 0.34 bar (5 psig). Figures 9a and 9b present the averaged normalized amplitudes and phase angles at increasing side feed pressures of 0.34 bar (5 psig), 1.4 bar (20 psig) and 2.8 bar (40 psig). The peak amplitude around the critical speed (ω_{cr}) increases for operation with side pressures of 1.4 bar (20 psig) and 2.8 bar (40 psig), thus implying a decrease in system damping ratio. Side pressurization does not change the system natural frequency, although the critical speed decreases slightly. Note that Ref. [8] shows somewhat opposite results, i.e. a reduction in the amplitudes of synchronous motion while crossing a critical speed. The discrepancy may be due to poor baseline imbalance subtraction in Ref. [8].
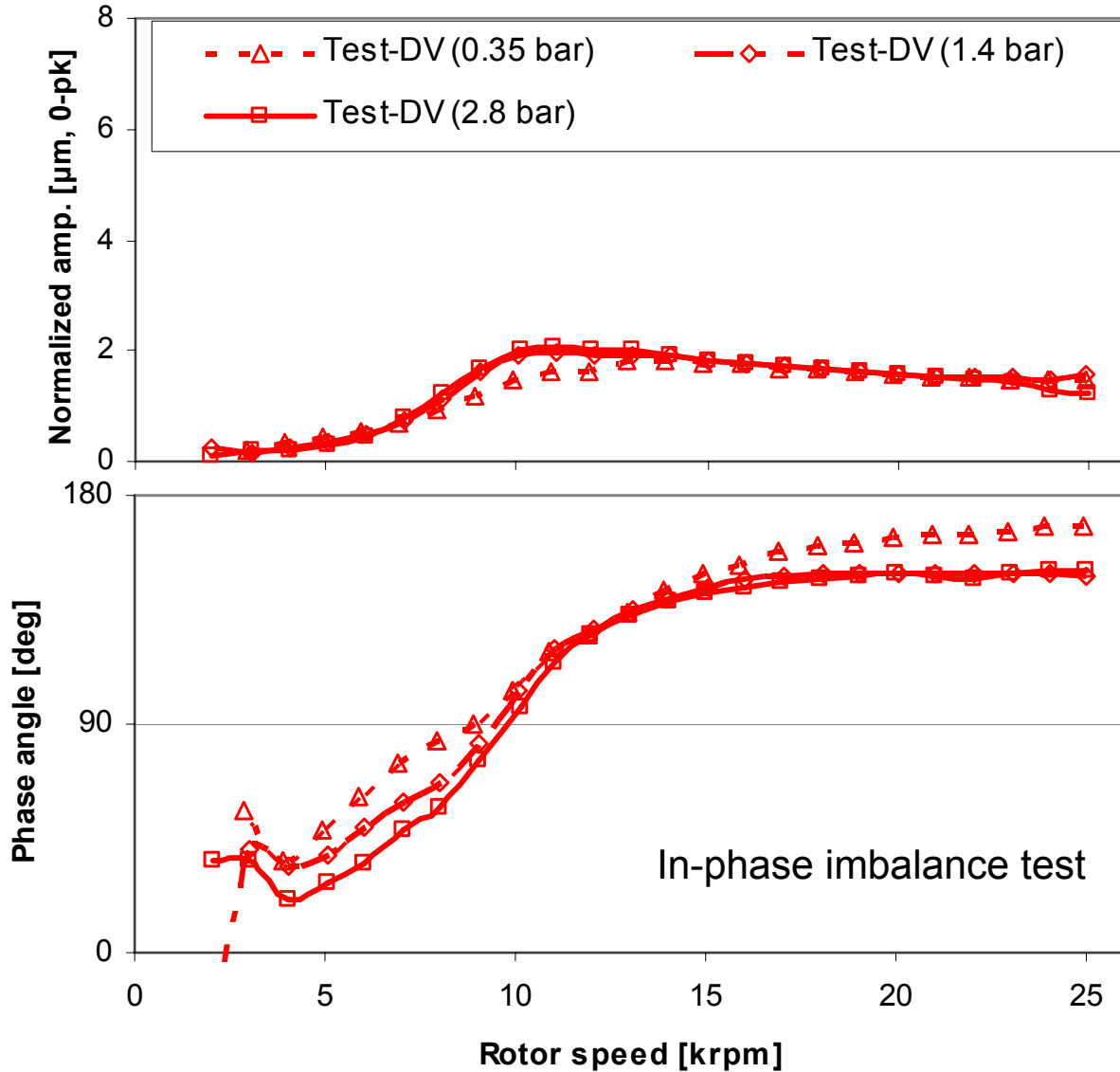
Figure 9a. Normalized rotor amplitude and phase angle of synchronous response (averaged over the increasing in-phase imbalance masses of 55 mg, 110 mg, and 165 mg) at increasing side gauge pressures of 0.34 bar (5 psig), 1.4 bar (20 psig), and 2.8 bar (40 psig). Measurement at drive end bearing, vertical plane with baseline subtraction. Original GFBs.
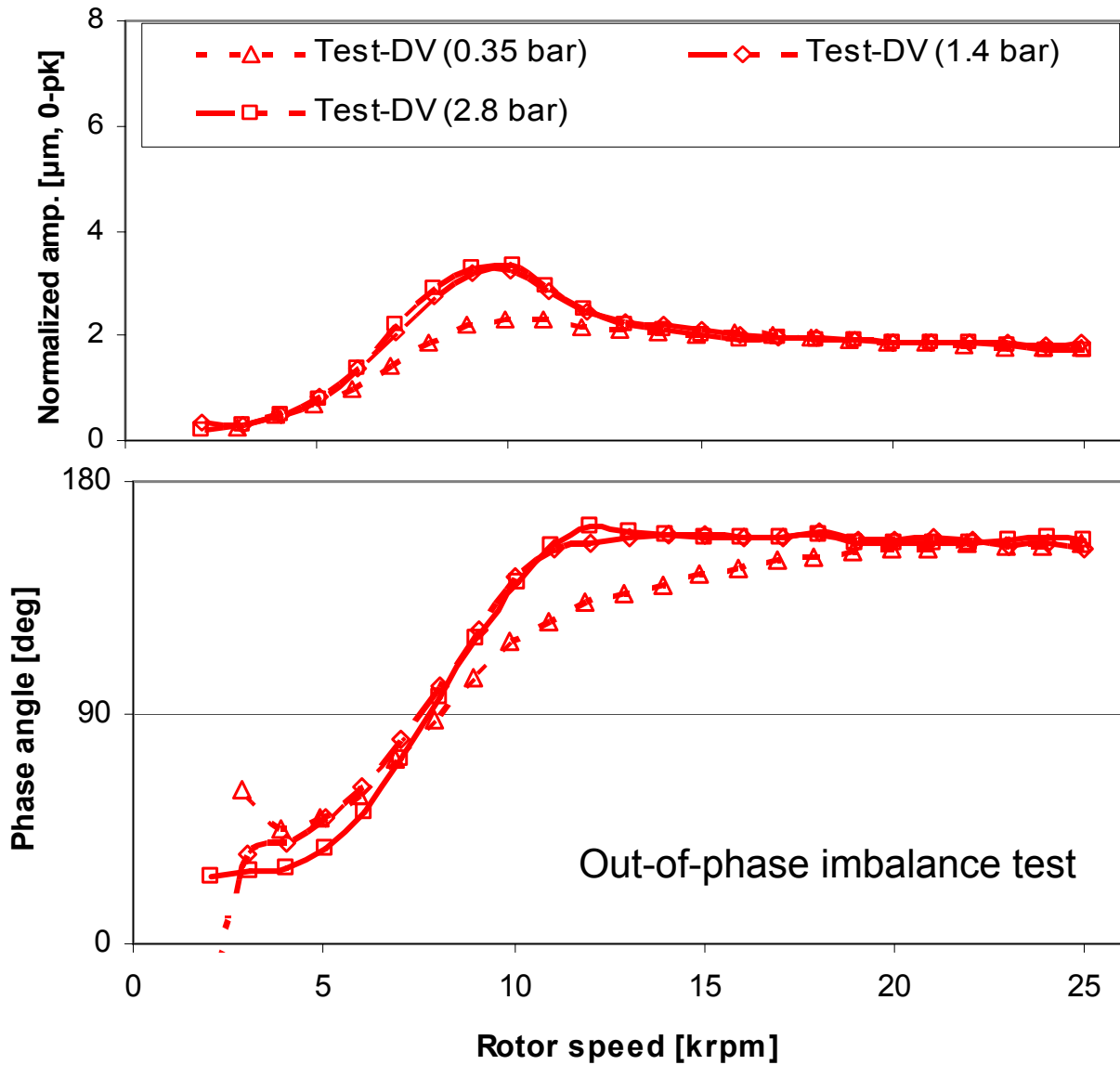
Figure 9b. Normalized rotor amplitude and phase angle of synchronous response (averaged over the increasing out-of-phase imbalance masses of 55 mg, 110 mg, and 165 mg) at increasing side gauge pressures of 0.34 bar (5 psig), 1.4 bar (20 psig), and 2.8 bar (40 psig). Measurement at drive end bearing, vertical plane with baseline subtraction. Original GFBs.

V. EFFECT OF MECHANICAL PRELOADS (SHIMS) ON DYNAMIC PERFORMANCE OF GFB

2006 TRC report [16] shows that the test rotor supported on the original GFBs could have operated to 50 krpm (motor maximum speed) for extended periods of time. The rotor showed significant subsynchronous motions from 27 krpm to 50 krpm for operation with a side air pressure at 0.34 bar (5 psig), see Fig. 10. As the rotor speed decreased from 50 krpm, the amplitudes of subsynchronous motions became smaller. In spite of the large rotor motions recorded for speeds larger than 27 krpm, the test GFBs survived without damage, except for some coating wear.

Three metal shims of 25 μm thickness are installed into the test GFB to enhance the bearing stiffness (See Table 2), and thus increasing the system critical speed. An increase in the critical speed is expected to increase the threshold speed of instability if the whirl frequency ratio (WFR) is unchanged. Coastdown tests from 50 krpm are conducted at a side feed pressure of 0.34 bar (5psig). Figure 11 displays the waterfall plot, synchronous and subsynchronous amplitudes, and subsynchronous whirl frequency of the vertical rotor motion recorded at the rotor free end for an out-of-phase imbalance mass of 110 mg. The amplitude of synchronous motion is smaller than 11 μm over the whole speed range. Significant subsynchronous motions appear from 50 krpm to ~ 40 krpm. The amplitude of the subsynchronous motions decreases with mechanical preload when compared to those without the mechanical preload. Below 40 krpm, the amplitude of the subsynchronous motions is smaller than 7 μm. Thus, introducing a preload in the GFBs delays by ~13 krpm the onset of subsynchronous motions with persistent increasing amplitudes of rotor motion. As rotor speed decreases from 50 krpm to 26 krpm, the subsynchronous whirl frequency decreases from 151 Hz to 137 Hz.
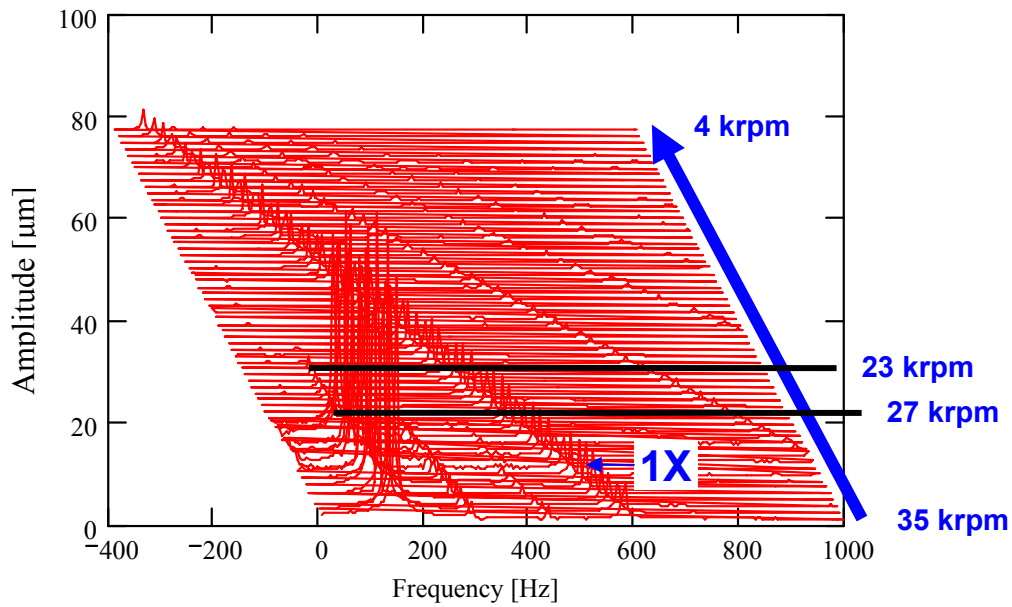
(a) Waterfall

(b) Synchronous and subsynchronous components

(c) Subsynchronous whirl frequency

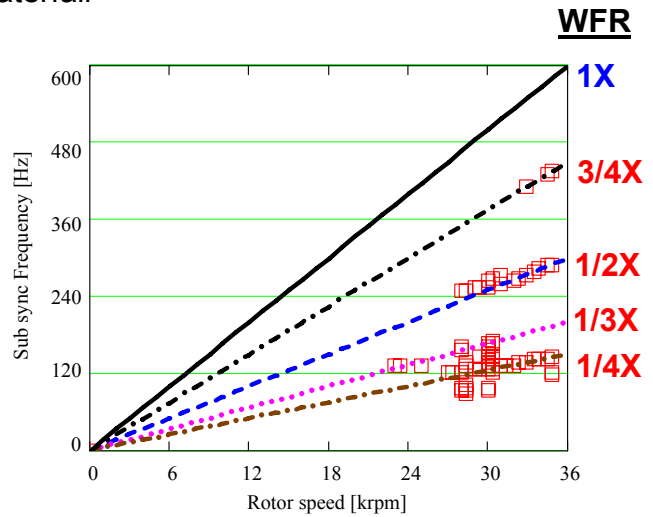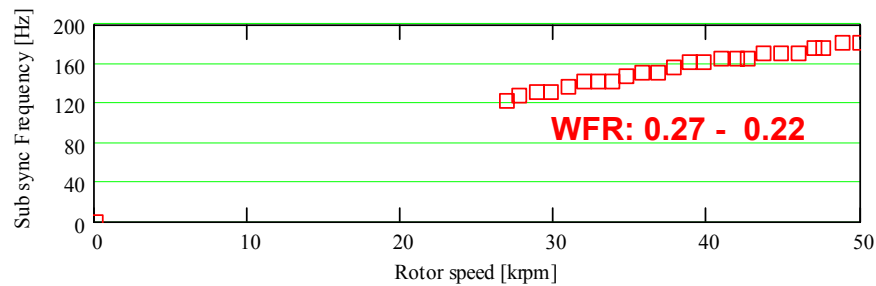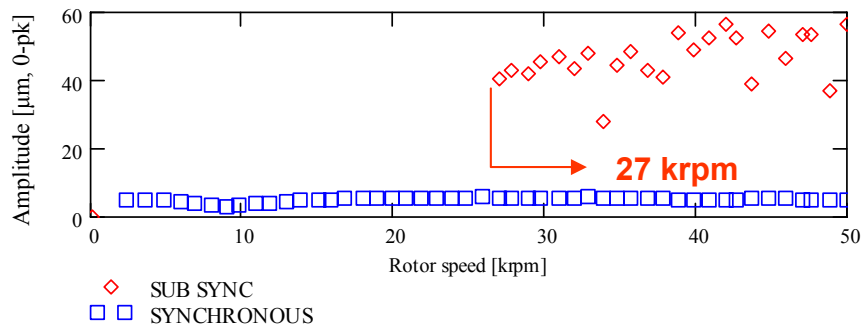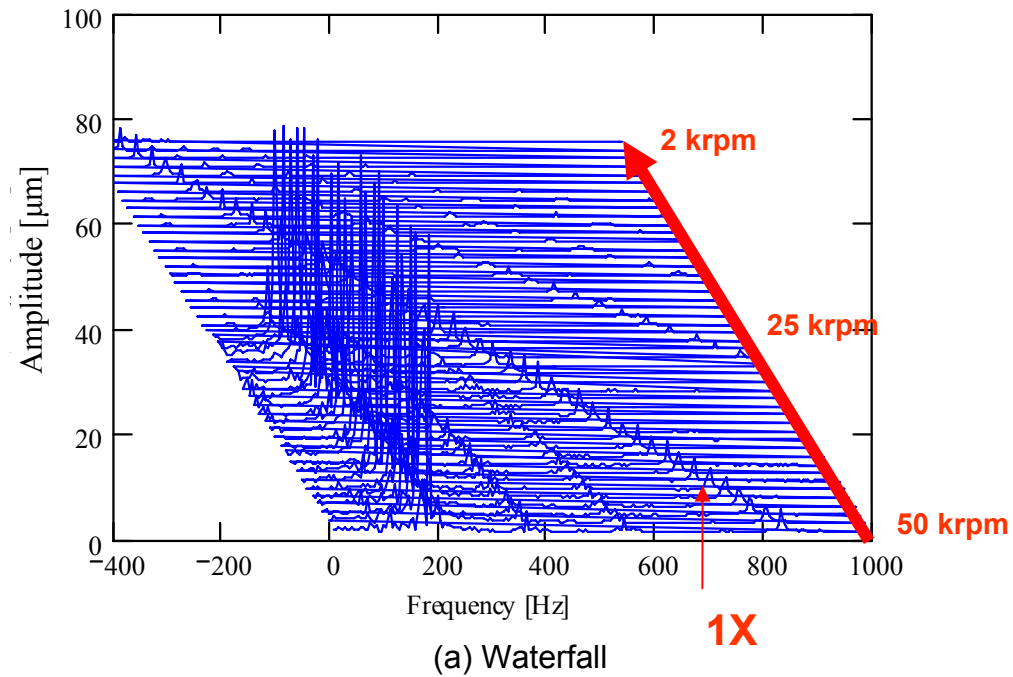**Figure 10. Coastdown rotor response from 50 krpm. Baseline imbalance condition, side air gauge pressure of 0.34 bar (5 psig). Measurement at rotor free end, vertical plane. Original GFBs [16].**
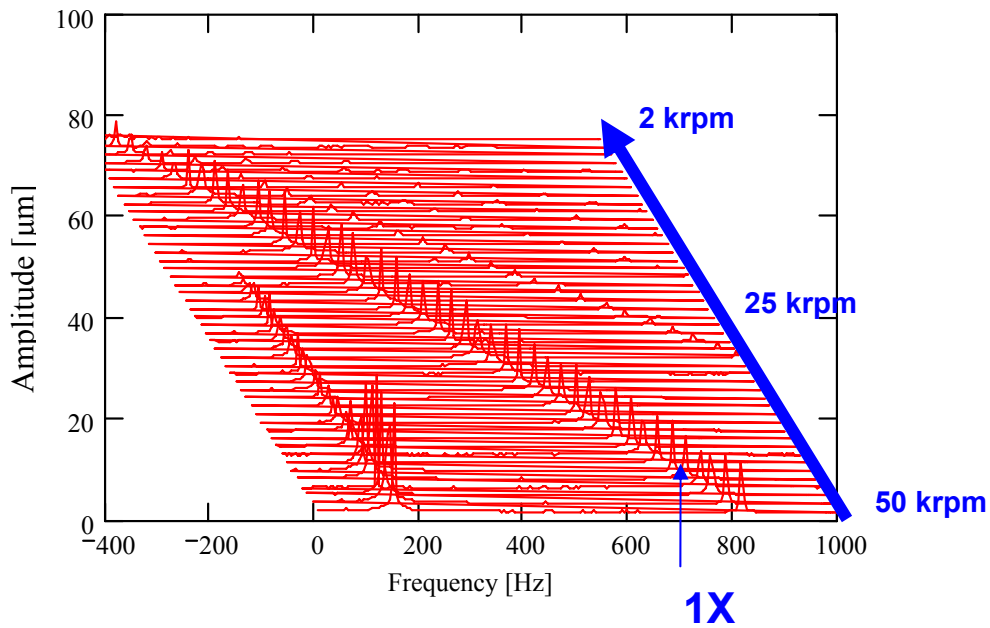
(a) Waterfall
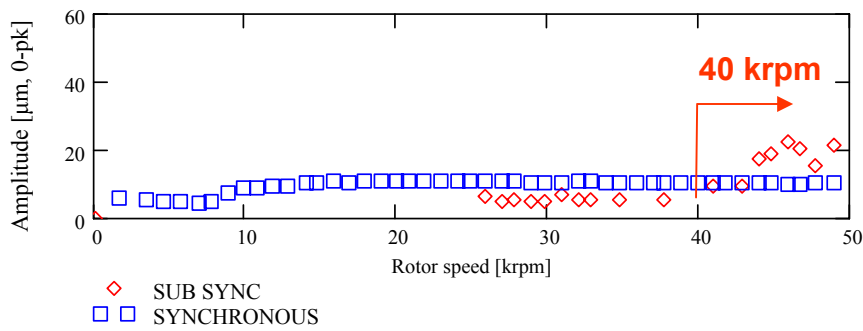
(b) Synchronous and subsynchronous components
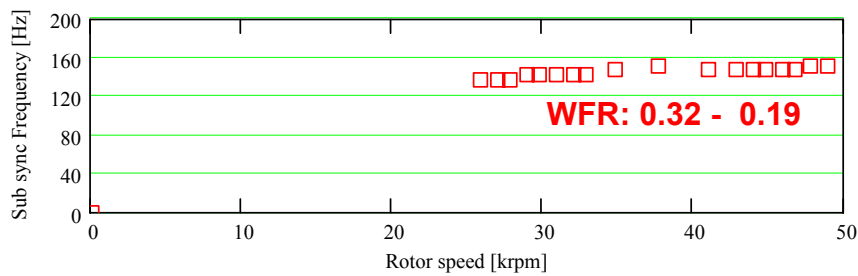
(c) Subsynchronous whirl frequency

Figure 11. Coast down rotor response from 50 krpm. Out of phase imbalance mass of 110 mg, side air gauge pressure of 0.34 bar (5 psig). Measurement at rotor free end, vertical plane. GFBs with shims.

Figure 12 displays the rotor coastdown responses from 50 krpm for GFBs supplied with an increased side pressure of 4.1 bar (60 psig), i.e., waterfall plot, synchronous and subsynchronous amplitudes, and subsynchronous whirl frequency of vertical motions recorded at the rotor free end. The amplitude of synchronous motion is smaller than 11 μm, and the subsynchronous motion appearing from 50 krpm to 27 krpm is smaller than 5 μm over the whole speed range. The subsynchronous whirl frequency decreases from 166 Hz to 142 Hz as the rotor speed decreases from 50 krpm to 30 krpm.

Figure 13 presents the amplitude of subsynchronous motion and associated whirl frequency measured during rotor speed-up tests for increasing side pressures. The rotor speed is manually controlled to accelerate the rotor from the minimum motor control speed (10 krpm) to the maximum motor speed (~50 krpm). The side feed pressure increases from 0.34 bar (5 psig) to 4.1 bar (60 psig) with a step increment of ~ 1.4 bar (20 psig) for each speed-up test. The measurements are taken at the rotor free end, vertical plane for out-of-phase imbalance of 110 mg. External pressurization reduces dramatically the amplitude of subsynchronous rotor motions. The subsynchronous whirl frequency does not change with air side pressurization, but increases from 142 Hz to 152 Hz as rotor speed increases.

Note that a moderate change in rotor imbalance condition does not have a discernable effect on the rotor response. See Appendix D for speed-up rotor responses from 10 krpm to 50 krpm for the baseline imbalance condition at side gauge pressures of 0.34 bar (5 psig) and 4.1 bar (60 psig).

(a) Waterfall

(b) Synchronous and subsynchronous components

(c) Subsynchronous whirl frequency
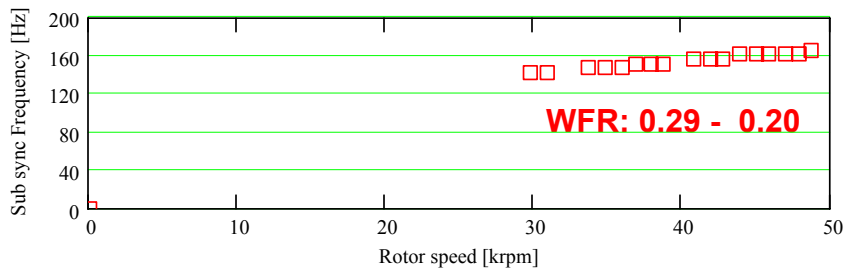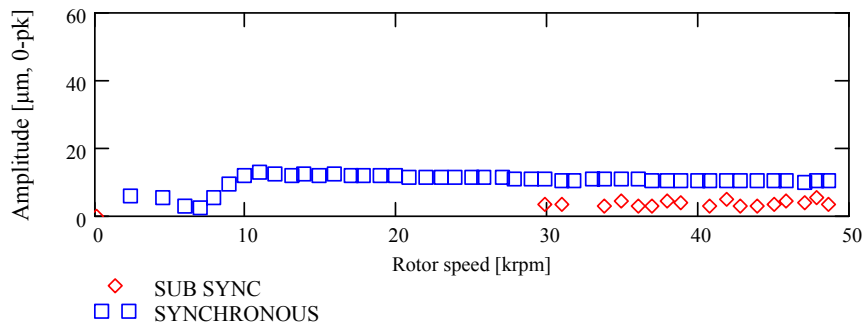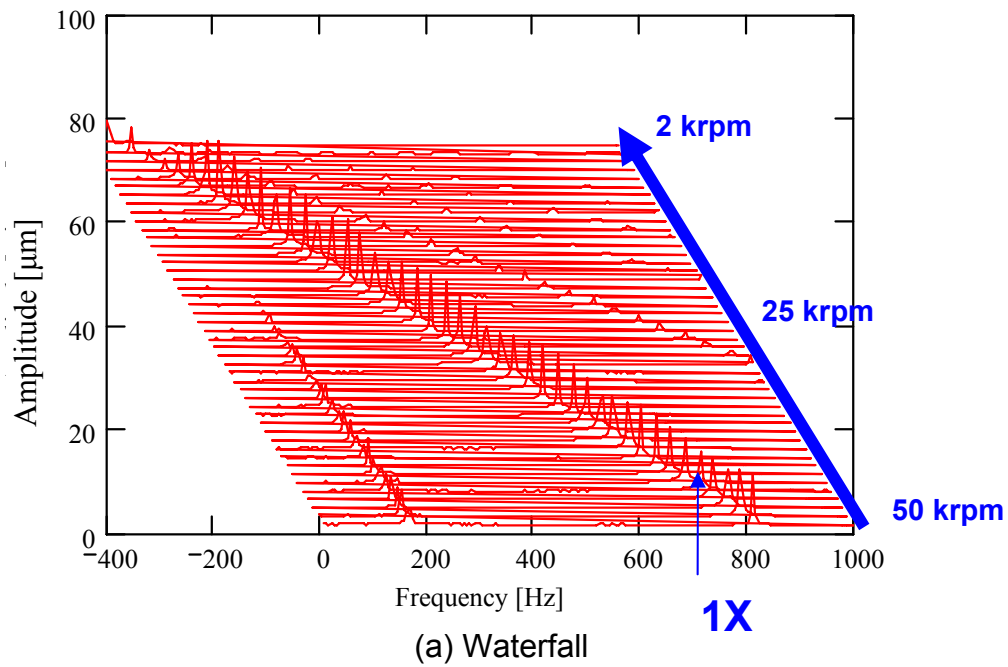
Figure 12. Coast down rotor response from 50 krpm. Out of phase imbalance mass of 110 mg, side air gauge pressure of 4.1 bar (60 psig). Measurement at rotor free end, vertical plane. GFBs with shims.
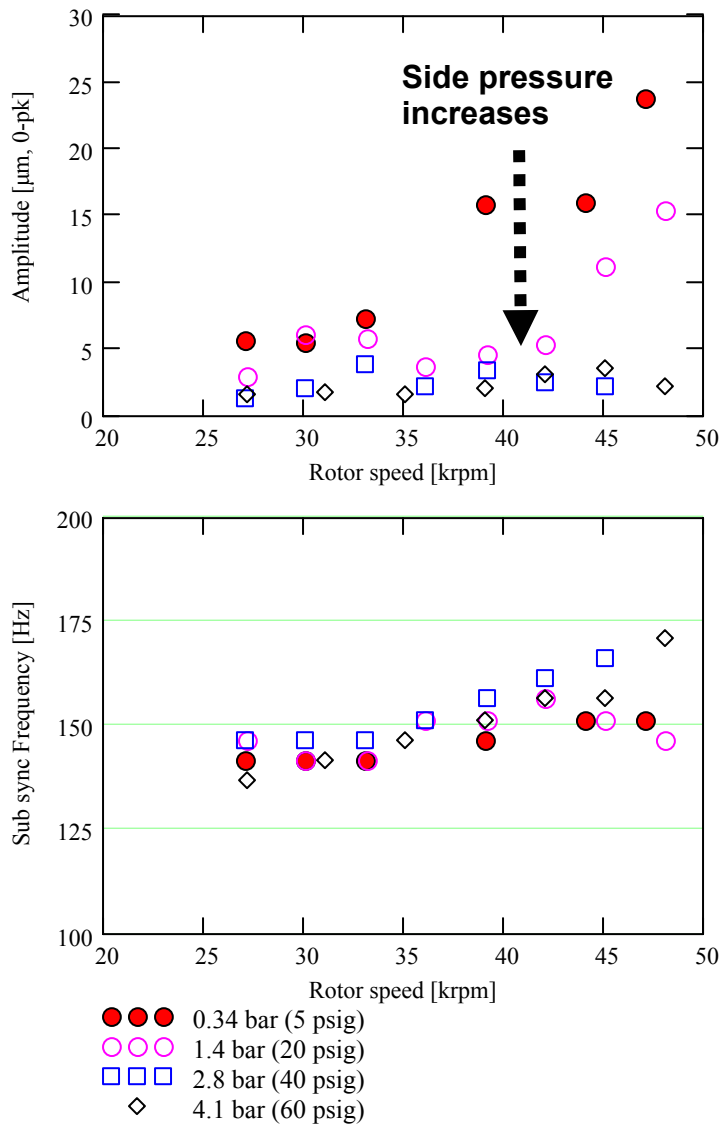
Figure 13. Amplitude of subsynchronous rotor motions, and subsynchronous whirl frequency during rotor speed-up test for increasing side pressurization. Out-of-phase imbalance mass of 110 mg. Measurement at rotor free end, vertical plane. GFBs with shims.

Rotor speed coastdown tests from 35 krpm are conducted with a side feed pressure of 0.34 bar (5psig) and the rotor at its baseline imbalance; and for in-phase and out-of-phase imbalance location conditions. Note that within this speed region (35 -0 krpm), subsynchronous rotor motions are insignificant. Figures 14a and 14b show normalized amplitudes of rotor synchronous response and phase angles for in-phase and out-of-phase imbalance masses equal to 55 mg and 110 mg.

The measurements at the rotor drive end, vertical plane are subtracted using the baseline synchronous response (amplitude and phase). The test data evidence nearly uniform normalized amplitudes, i.e., characteristics of a linear system as reported for GFBs. The natural frequency (ω_n) increases by ~ 5 krpm at the drive end bearing (vertical plane) for an in-phase imbalance mass of 55 mg; when compared to that for the GFB without shims. The increase in natural frequency (9 krpm → 14 krpm) implies an increase in bearing direct stiffness due to the mechanical preload.

Appendix E displays the normalized amplitude and phase angle of the rotor synchronous response for the free end bearing, vertical plane. Appendix F lists the dynamic parameters of the rotor-GFB system identified using the synchronous response for GFBs with shims. In general, installation of shims significantly increases the effective stiffness (K_{eff}) and decreases the damping ratio (ξ) and effective damping (C_{eff}). However, K_{eff} decreases notably for the imbalance mass of 110 mg when compared to that with the small imbalance mass of 55 mg. A reduction in K_{eff} is rather significant for the drive end GFB which has a smaller nominal radial clearance than the free end GFB[4]. Recall that K_{eff} is not sensitive to the smallest to moderate imbalance masses for the original configuration of GFBs without shims, as discussed in Appendix B.

---

4 See Appendix G for the estimated nominal radial clearances of the drive and free end GFBs, original configuration (without shims).
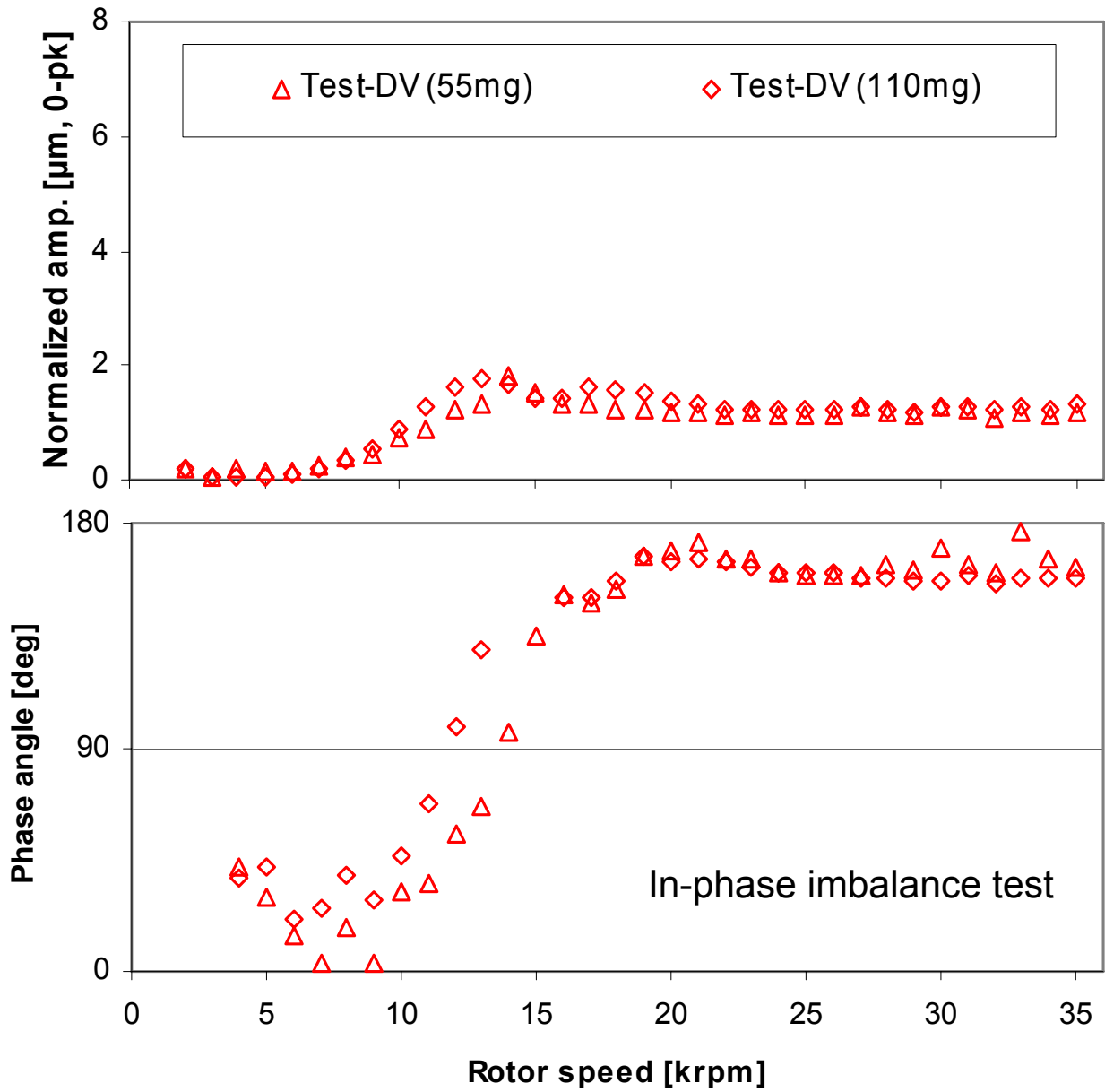
Figure 14a. Normalized amplitude of synchronous response and phase angle for in-phase imbalance masses of 55mg and 110mg. Measurements at drive end bearing, vertical plane with baseline subtraction. Side air gauge pressure at 0.34 bar (5 psig). GFBs with shims.
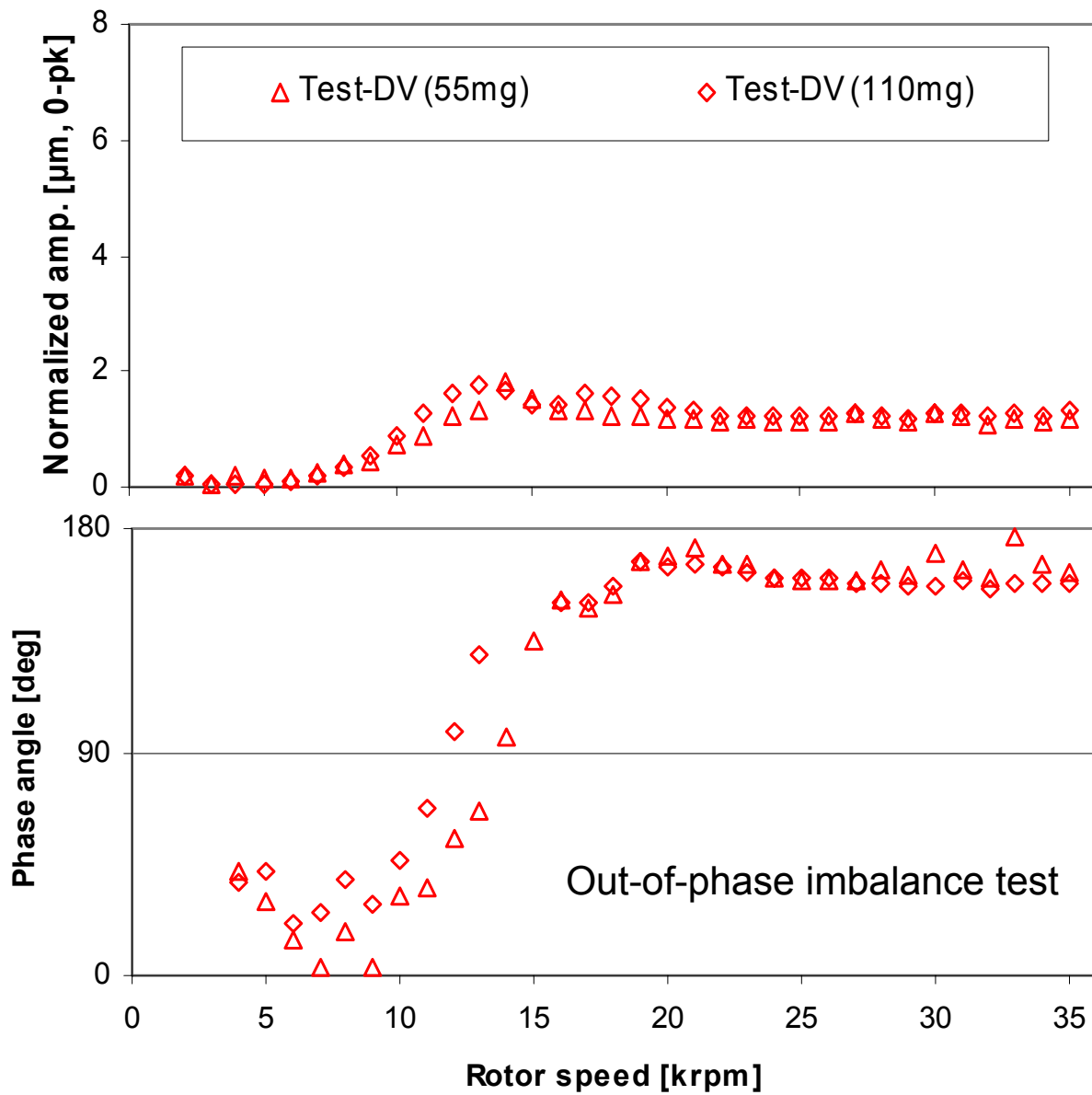
Figure 14b. Normalized amplitude of synchronous response and phase angle for out-of-phase imbalance masses of 55mg and 110mg. Measurements at drive end bearing, vertical plane with baseline subtraction. Side air gauge pressure at 0.34 bar (5 psig). GFBs with shims.

Figures 15a and 15b compare the amplitudes and phase angle of rotor synchronous motions at feed gauge pressures of 0.34 bar (5 psig) and 4.1 bar (60 psig) for the out-of-phase imbalance condition. The measurements recorded during coastdown tests show the subtraction of the baseline synchronous response (amplitude and phase). The speed coastdown test at 4.1 bar (60 psig) is conducted from 50 krpm; while the coastdown test at 0.34 bar (5 psig) is conducted from 38 krpm to reduce the influence of subsynchronous motions on the amplitude of the synchronous motion. A comparison of the synchronous amplitudes does not show significant changes for increasing side feed pressures, i.e. critical speed and natural frequency are similar for the measurements at the drive and free end GFBs. However, for the measurement at the free end GFB, vertical plane, the amplitude increases from 3.5 μm to 5.8 μm, implying a reduction in damping. In general, side pressurization may reduce damping while crossing a critical speed. This observation is valid for both the original and shimmed GFBs.
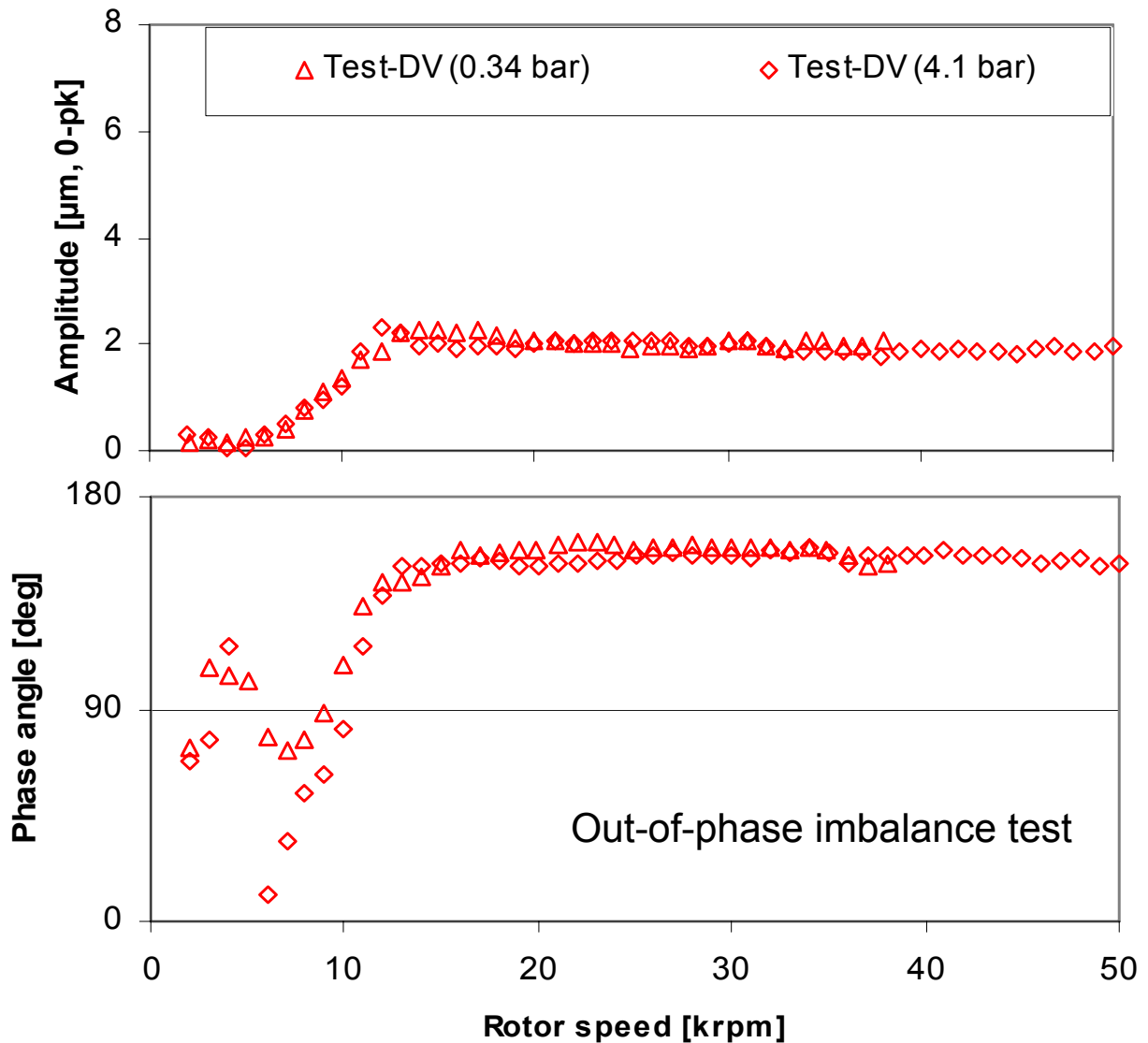
Figure 15a. Amplitude and phase angle of synchronous rotor motion versus rotor speed for side gauge pressures of 0.34 bar (5 psig) and 4.1 bar (60 psig). Measurements at drive end, vertical plane. Out-of-phase imbalance mass of 110 mg with baseline subtraction. GFBs with shims.
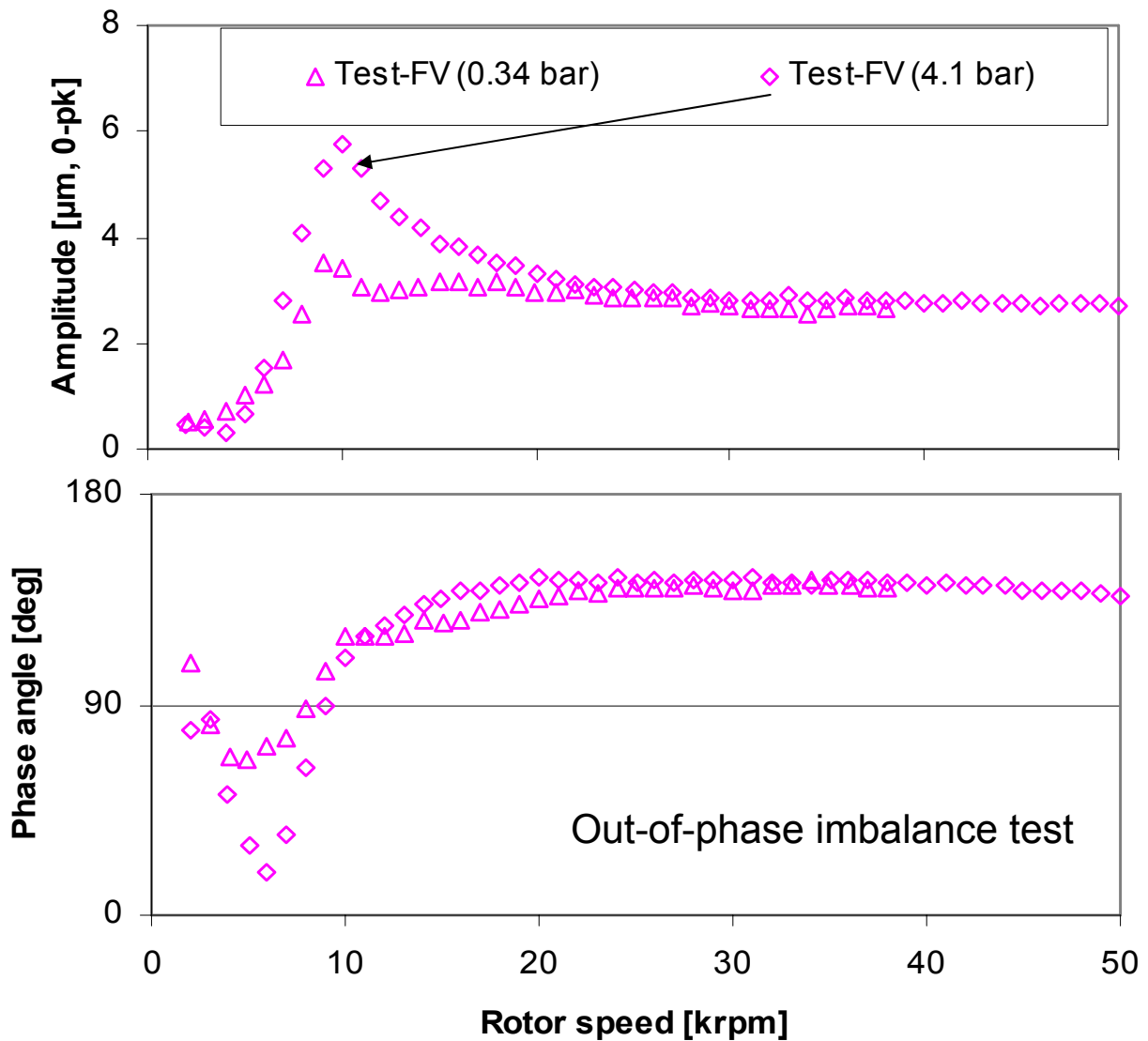
Figure 15b. Amplitude and phase angle of synchronous rotor motion versus rotor speed for side gauge pressures of 0.34 bar (5 psig) and 4.1 bar (60 psig). Measurements at free end, vertical plane. Out-of-phase imbalance mass of 110 mg with baseline subtraction. GFBs with shims.

The static locus of the rotor centerline for increasing rotor speeds is estimated for the test GFBs. For GFBs with side pressurization, the measurements may guide advancements in predictive models by providing an insight into the static performance of GFBs operating at increasing rotor speeds. Because a bearing geometric center, as well as the bearing clearance, is generally unknown, the initial rotor center position is set to zero. The DC bottom line refers to the locations where the rotor is in contact with the test bearings and without rotor spinning. Note that this bottom line may be relatively accurate for the free end bearing, while it may not be for the drive end bearing due to the flexible coupling connected to the rotor drive end. Appendix G displays the estimation of the flexible coupling stiffness.

Figure 16 displays the trajectory of the rotor static center during speed-up tests for an out of phase imbalance mass of 110 mg. Square and diamond symbols indicate measurements at the rotor drive and free ends, respectively. As the rotor speed increases from 11 krpm to 50 krpm, the static centerline measured at the rotor free end moves up and left, in a path with the same orientation as rotor spinning. At the rotor drive end, the orbit center moves up and right, in a path opposite to the orientation of rotor spinning. Hence, both the rotor static centers at the rotor drive and free ends moves up, in paths with different orientations as the rotor speed increases. As the side pressure increases, the trajectory measured at the rotor free end tends to move up and the movement in the horizontal direction becomes narrower. The trajectory measured at the rotor drive end moves down slightly and the movement in the horizontal direction becomes narrower. Note that the rotor has a small static displacement at the rotor drive end due to the coupling force. Relatively larger stiffness and smaller nominal clearance for the drive end GFB to those for the free end GFB (see Appendix G) also restrain the static displacement at the rotor drive end.
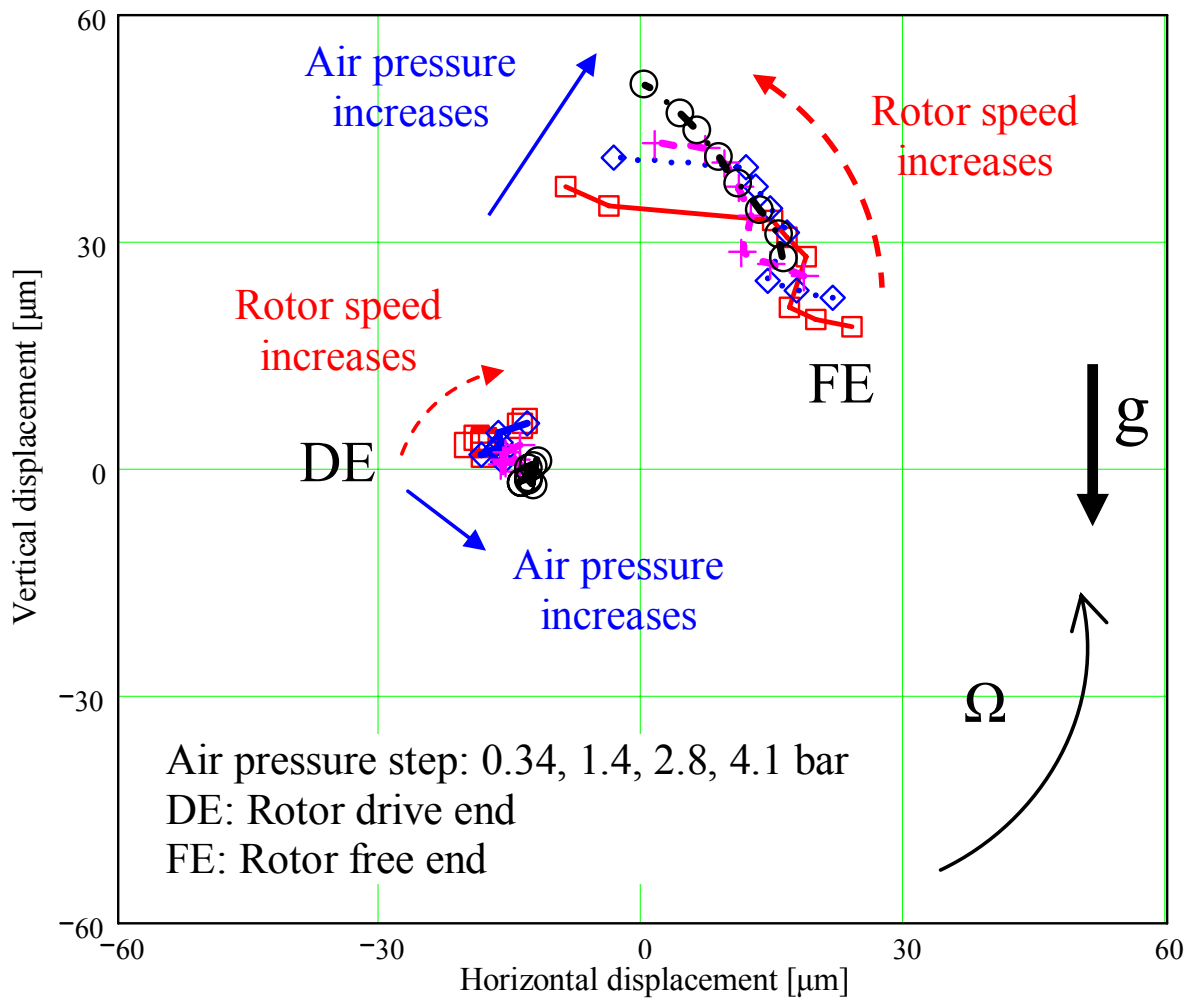
Figure 16. Trajectory of rotor center during speed-up tests with increasing side pressures. Speed-up responses from 11 krpm to 50 krpm. DC-offset subtraction. Out-of-phase imbalance mass of 110 mg. Measurement at rotor drive and free ends. GFBs with shims.

Figure 17 compares the static trajectories of the rotor center during rotor speed coastdown tests from 50 krpm for side gauge pressures of 0.34 bar and 4.1 bar and an out of phase imbalance mass of 110 mg. As the rotor speed decreases, the static rotor center measured at the rotor free end moves down and right, in a path opposite to the orientation of rotor spinning. On the other hand, the rotor center measured at the rotor drive end moves down and left, in a path with the same orientation as rotor spinning. With increased pressure, the trajectory measured at the rotor free end moves up and the movement in the horizontal direction becomes narrower. Thus, it is inferred that an increase in side pressure may reduce the cross-coupled effects destabilizing the rotor at high speeds.
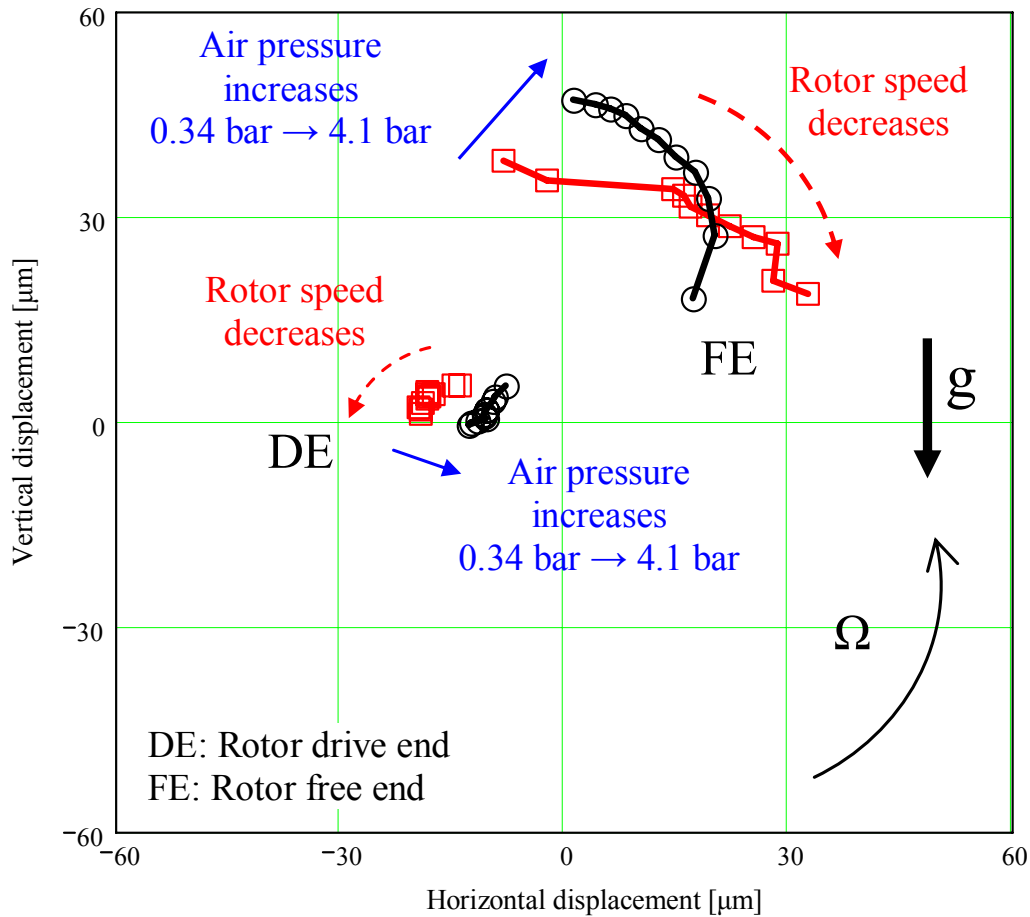
Figure 17. Trajectory of rotor center during rotor coastdown tests from 50 krpm with side gauge pressures of 0.34 bar and 4.1 bar. DC-offset subtraction. Out-of-phase imbalance mass of 110 mg. Measurement at rotor drive and free ends. GFBs with shims.

Figure 18 displays the rotor speed versus time for the modified GFB with mechanical preload (shims) operating with side feed gauge pressures of 0.34 bar and 4.1 bar (baseline imbalance). The results are compared to those for the original GFBs (without shims) at a side feed gauge pressure of 0.34 bar [16]. In general, all results display an exponential decay of rotor speed with time from 50 krpm to 10 krpm, thus implying an operation with "viscous" drag. From 5 krpm until rest, rotor operation shows dry friction effects (rotor rubs) with a fast deceleration to rest. Note that the rotor may touch down earlier in shimmed GFBs, at 0.34 bar gauge, because of the bearings' smaller clearances.
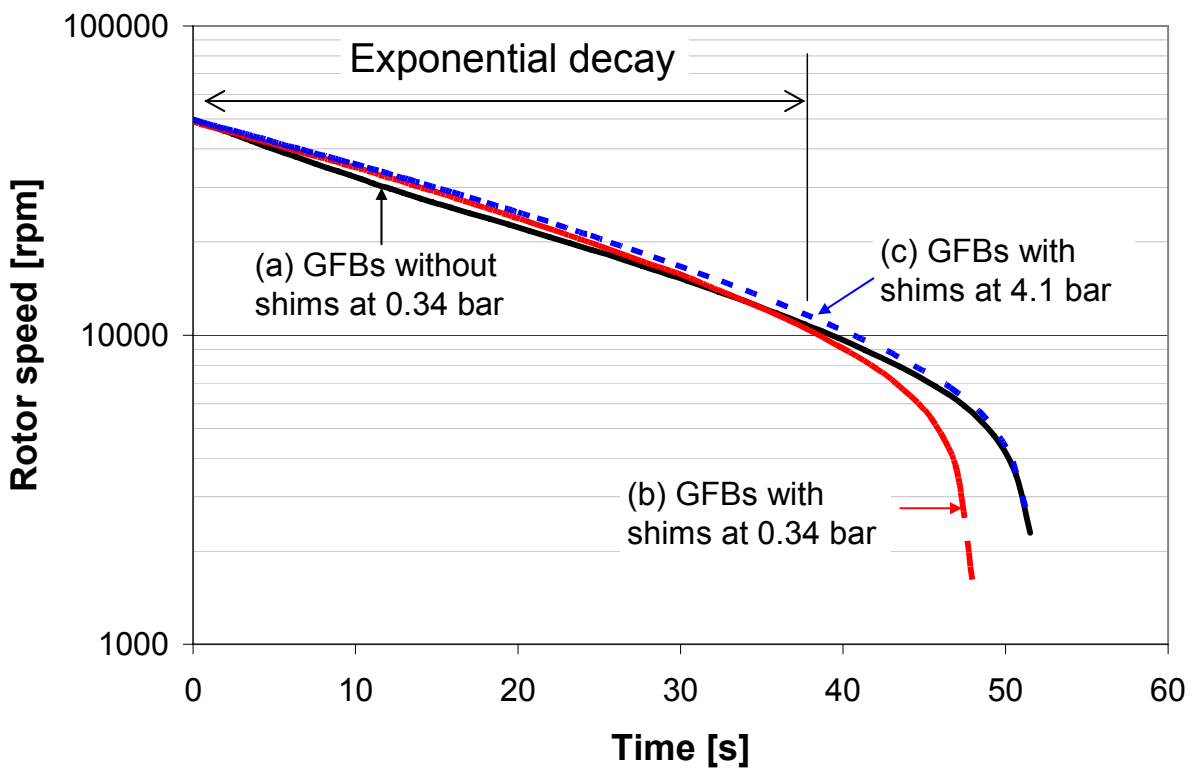
Figure 18. Rotor speed versus time during coastdown tests from 50 krpm for the original GFBs and the GFBs with shims. Baseline imbalance condition for (a) and (c). Out of phase imbalance mass of 110 mg for (b).

VI. CONCLUSIONS

Rotordynamic response measurements of a test rotor supported on GFBs are conducted during rotor speed-up and coastdown tests. The GFBs are fed with side air gauge pressures to 4.1 bar (60 psig). Side pressurization demonstrates the dramatic effect of side gas pressurization on reducing the total amplitude of motions, mainly composed of subsynchronous whirl frequencies. For sufficiently high side feed pressures into the bearings, the shaft subsynchronous whirl motions disappear; i.e. the test system becomes rotordynamically stable. At a side feed pressure of 0.34 bar (5 psig), coastdown rotor responses from 25 krpm and for large imbalance conditions show an increase in normalized peak amplitudes of synchronous response and at a lower critical speed, due to a reduction in equivalent viscous damping, when compared to those for small to moderate imbalance conditions.

Installation of metal shims under the foil bearing bump strip layers and in contact with the bearing cartridge introduces mechanical preload into the test GFBs. The preload increases the threshold speed of instability where subsynchronous motions suddenly appear with large amplitudes. Bearing side pressurization to 4.1 bar (60 psig) significantly delays this threshold speed. Estimated loci of static rotor centerline show that side pressurization aids to reduce cross-coupled effects that destabilize the rotor-bearing system at high rotational speeds. Rotor speed versus time measurements obtained during coastdown tests, 50 krpm to 10 krpm, for the original GFBs and shimmed GFBs display an exponential decay, thus evidencing an operation with small "viscous" drag.

As a final observation, although external pressurization aids to better the rotordynamic performance of the test rotor supported on GFBs; in an actual high temperature application, a too large cooling flow rate may penalize sensibly the efficiency and performance of the turbomachinery supported on GFBs.

VII. REFERENCES

[1] Agrawal, G. L., 1997, "Foil Air/Gas Bearing Technology – an Overview," ASME Paper No. 97-GT-347.

[2] Heshmat, H., Walowit, J. A., and Pinkus, O., 1983, "Analysis of Gas-Lubricated Foil Journal Bearings," ASME J. Lubr. Tech., **105**, pp. 647-655.

[3] San Andrés, L., 1995, "Turbulent Flow Foil Bearings for Cryogenic Applications," ASME J. Tribol., **117**, pp. 185-195.

[4] Blok, H., and van Rossum, J. J., 1953, "The Foil Bearing – A New Departure in Hydrodynamic Lubrication," Lubr. Eng., December, pp. 316-320.

[5] DellaCorte, C., and M., Valco, 2000, "Load Capacity Estimation of Foil Air Journal Bearing for Oil-Free Turbomachinery Applications," STLE Tribol. Trans., **43**(4), pp. 795-801.

[6] Lubell, D., DellaCorte, C. and Stanford, M., 2006, "Test Evolution and Oil-Free Engine Experience of a High Temperature Foil Air Bearing Coating," ASME Paper No. GT2006-90572.

[7] Bauman, S., 2005, "An Oil-Free Thrust Foil Bearing Facility Design Calibration, and Operation," NASA/TM-2005-213568.

[8] San Andrés, L., D. Rubio, and T.H. Kim, 2006, "Rotordynamic Performance of a Rotor Supported on Bump Type Foil Gas Bearings: Experiments and Predictions," ASME Paper No. GT 2006-91238 (to appear in ASME J. Eng. Gas Turbines and Power, **129**, 2007).

[9] Chen, H. M., Howarth, R. Geren, B., Theilacker, J. C., and Soyars, W. M., 2000, "Application of Foil Bearings to Helium Turbocompressor," *Proc. 30th Turbomachinery Symposium*, Texas A&M Univ., Houston, TX, pp. 103-113.

[10] Heshmat, H., Shapiro, W., and Gray, S., 1982, "Development of Foil Journal Bearings for High Load Capacity and High Speed Whirl Stability," ASME J. Lubr. Tech., **104**, pp. 149-156.

[11] Kim, T.H., and L. San Andrés, 2006, "Limits for High Speed Operation of Gas Foil Bearings," ASME J. Tribol., **128**, pp. 670-673.

[12] Ruscitto, D., Mc Cormick, J., and Gray, S., 1978, "Hydrodynamic Air Lubricated Compliant Surface Bearing For An Automotive Gas Turbine Engine I-Journal Bearing Performance," NASA CR-135368.

[13] Heshmat, H., 1994, "Advancements in the Performance of Aerodynamic Foil Journal Bearings: High Speed and Load Capacity," ASME J. Tribol., **116**, pp. 287-295.

[14] San Andrés, L., and Kim, T. H., 2006, "Computational Analysis of Gas Foil Bearings Integrating 1D and 2D Finite Element Models for Top Foil," Technical Report No. TRC-B&C-1-06, Texas A&M Univ., College Station, TX.

[15] San Andrés, L., and T-H Kim, 2007, "Improvements to the Analysis of Gas Foil Bearings: Integration of Top Foil 1D and 2D Structural Models," ASME Paper No. GT2007-27249 (to be presented at Turbo-Expo Conference, Montreal, Canada, 2007, May)

[16] San Andrés, L., and Kim, T.H, 2006, "Further Imbalance Response Measurements of Rotor Supported on Bump-Type Gas Foil Bearings: Operation to 50 krpm," Technical Report No. TRC-B&C-1-06, Texas A&M Univ., College Station, TX.

[17] Rubio, D., and San Andrés, L., 2007, "Structural Stiffness, Dry Friction Coefficient, and Equivalent Viscous Damping in a Bump-Type Foil Gas Bearing," ASME J. Eng. Gas Turbines Power, **129**, pp. 494-502.

[18] Ginsberg, J. H., 2001, *Mechanical and Structural Vibration – Theory and Application*, John Wiley & Sons, New York, pp. 135–139.

APPENDIX A. Normalized amplitude and phase angle of synchronous response at free end bearing, vertical plane: Original GFBs.

Figure A1a. Influence of large imbalance mass on normalized amplitude and phase angle of synchronous response. In-phase imbalance masses of 55mg, 110mg, 165mg, and 330mg. Measurement at free end bearing, vertical plane with baseline subtraction. Side gauge pressure at 0.34 bar (5 psig). Original GFBs.
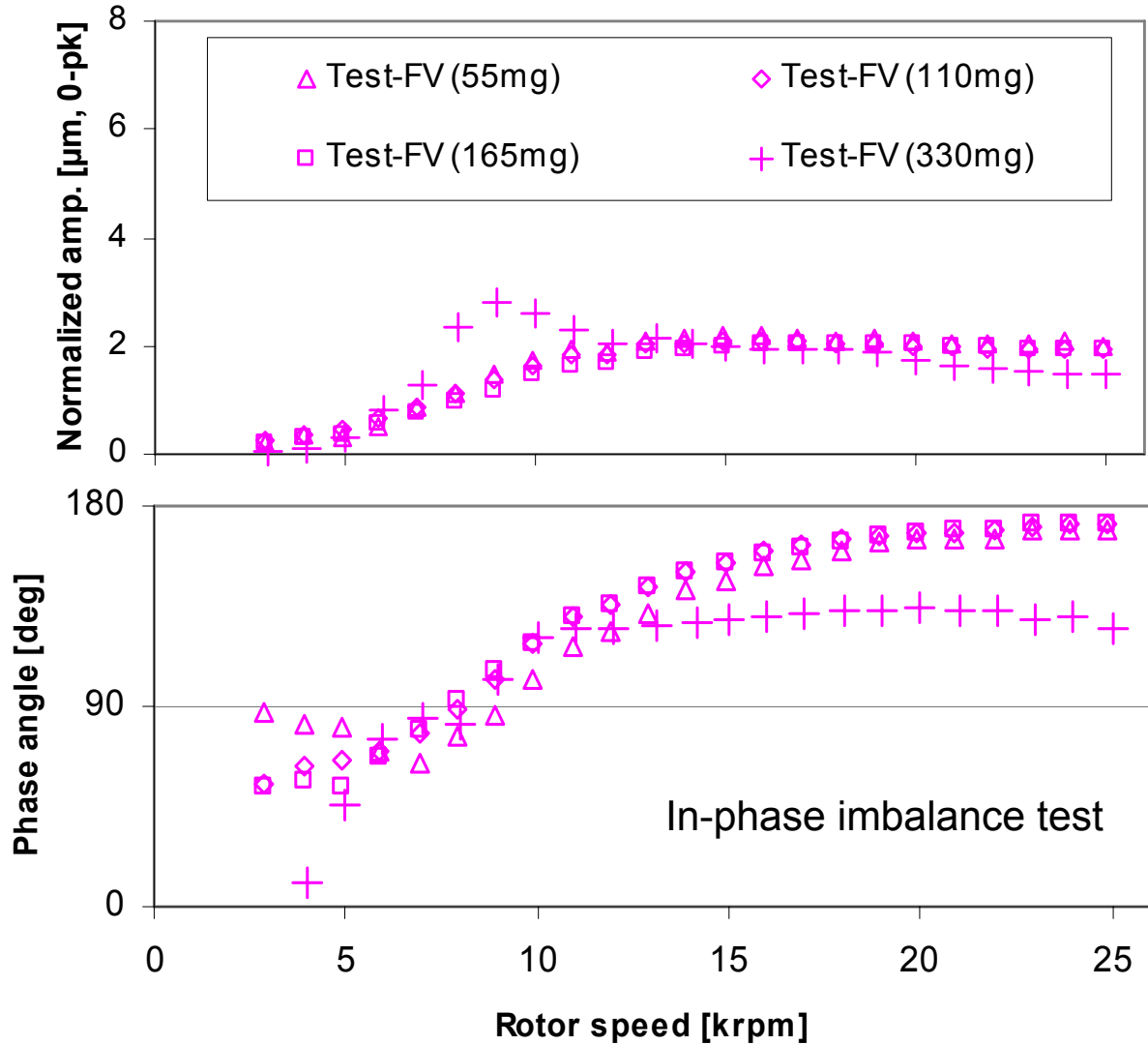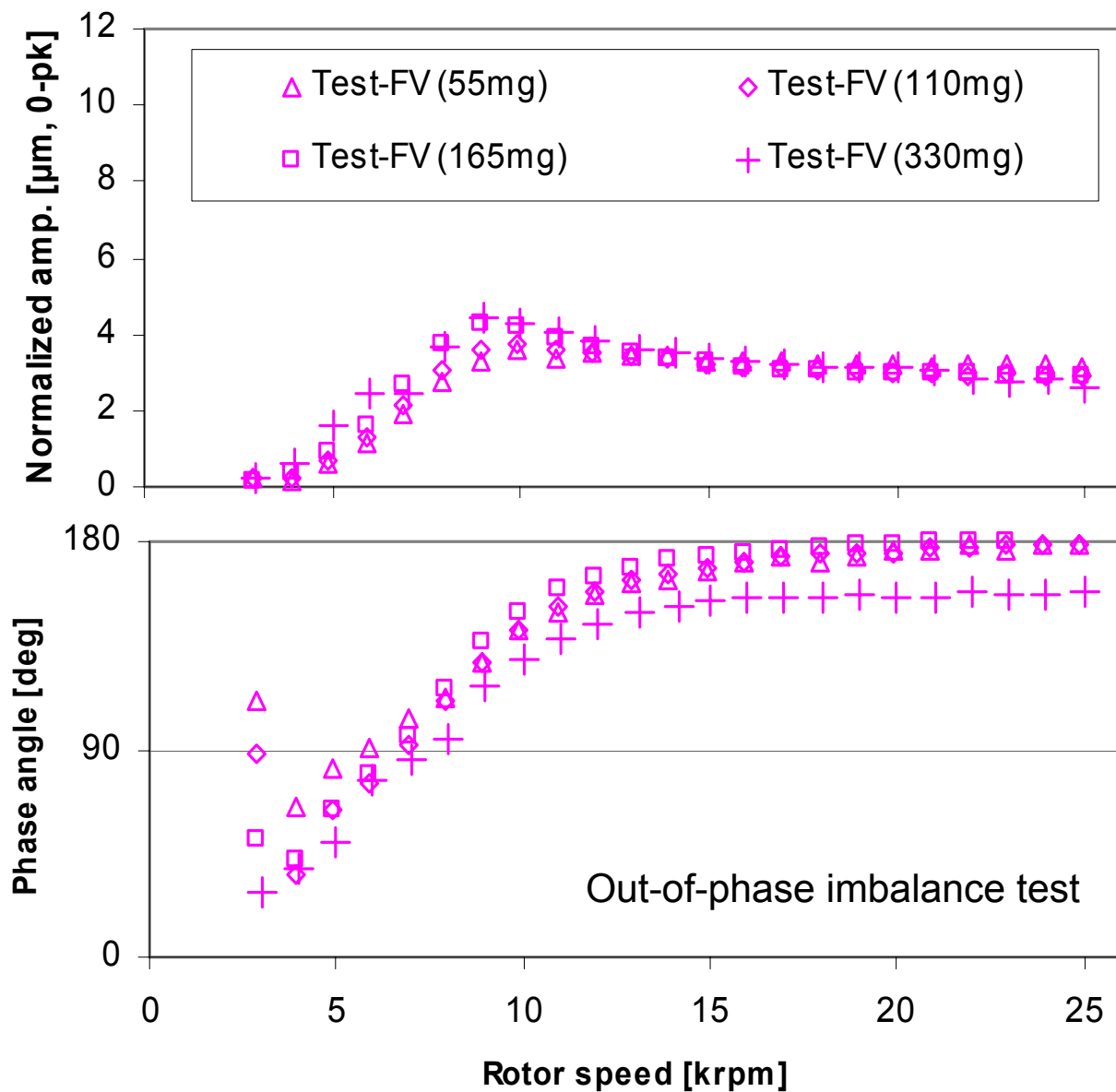
Figure A1b. Influence of large imbalance mass on normalized amplitude and phase angle of synchronous response. Out-of-phase imbalance masses of 55mg, 110mg, 165mg, and 330mg. Measurement at free end bearing, vertical plane with baseline subtraction. Side gauge pressure at 0.34 bar (5 psig). Original GFBs.

APPENDIX B. Rotordynamic parameters of the rotor and GFBs: Original GFBs.

Rotordynamic parameters of the rotor-GFB system are identified using a one degree of freedom model. Phase angles equal to 90 º identify the undamped natural frequencies, ω_n, for in-phase and out-of-phase imbalance conditions. The effective stiffness coefficient, K_{eff} is estimated as $K_{eff} = \omega_n^2 M$ at the drive and free end bearing locations. Note that M is a fraction of the rotor mass that each bearing supports. The damping ratio (ξ) and the damping coefficient (C_{eff}) are estimated as [18];

$$\xi = \sqrt{\frac{1}{2}\left\{1-\left(\frac{\omega_n}{\omega_{cr}}\right)^2\right\}} \; ; \qquad C_{eff} = 2\xi\sqrt{K_{eff} M} \qquad \text{(B-1)}$$

Note that, in the first equation above, the damping ratio (ξ) approaches zero as the critical speed, ω_{cr} moves toward the natural frequency, ω_n. Hence, Table B1 lists the dynamic parameters of the rotor-GFB system identified, using the synchronous response for the moderate imbalance mass of 110 mg and the large imbalance mass of 330 mg. Note that small to moderate imbalance masses of 55 mg, 110 mg, and 165 mg result in nearly uniform normalized amplitude and phase angle of synchronous response, thus implying no discernable difference in dynamic parameters of the rotor-GFB system. For the small to moderate imbalance masses, the damping ratios are ~ 0.5 for the in-phase and out-of-phase imbalance conditions, thus implying a well-damped system. On the other hand, with the large imbalance mass of 330 mg, the damping ratio is smaller than 0.3 for most estimations. Note that, in this simple analysis, K_{eff} and C_{eff} may not accurately represent the bearing stiffness and damping coefficients due to the influence of the coupling stiffness.

Table B1. Estimated rotordynamic parameters of the rotor-GFB system obtained from synchronous coastdown responses. Side air gauge pressure at 0.34 bar (5 psig): Original GFBs.

Location		Imbalance Condition	Natural frequency, $\omega_n\times(30/\pi)$ [rpm]	Critical Speed, $\omega_{cr}\times(30/\pi)$ [rpm]	Effective stiffness, K_{eff} [MN/m]	Damping ratio, ξ	Effective damping, C_{eff} [N-s/m]
Imbalance mass (55 mg), u_{DE} = 1.26 μm and u_{FE} = 2.34 μm							
Drive end	X_{DE}	in phase	9,000	13,000	0.59	0.51	635
		out of phase	7,000	11,000	0.35	0.55	528
	Y_{DE}	in phase	10,000	18,000	0.72	0.59	813
		out of phase	8,000	11,000	0.46	0.49	537
Free End	X_{FE}	in phase	9,000	15,000	0.32	0.57	384
		out of phase	6,000	10,000	0.14	0.57	256
	Y_{FE}	in phase	10,500	16,000	0.44	0.53	422
		out of phase	9,000	15,000	0.32	0.57	384
Imbalance mass (110 mg), u_{DE} = 2.52 μm and u_{FE} = 4.67 μm							
Drive end	X_{DE}	in phase	9,000	13,000	0.59	0.51	635
		out of phase	7,000	11,000	0.35	0.55	528
	Y_{DE}	in phase	8,500	18,000	0.52	0.62	732
		out of phase	8,000	11,000	0.46	0.49	537
Free End	X_{FE}	in phase	8,000	16,000	0.25	0.61	369
		out of phase	7,000	10,000	0.19	0.51	267
	Y_{FE}	in phase	8,000	16,000	0.25	0.61	369
		out of phase	8,500	12,000	0.29	0.50	320
Imbalance mass (165 mg), u_{DE} = 3.78 μm and u_{FE} = 7.00 μm							
Drive end	X_{DE}	in phase	9,000	13,000	0.59	0.51	635
		out of phase	7,000	10,000	0.35	0.51	489
	Y_{DE}	in phase	8,500	18,000	0.52	0.62	732
		out of phase	6,500	10,000	0.31	0.54	483
Free End	X_{FE}	in phase	8,000	18,000	0.25	0.63	382
		out of phase	7,000	9,000	0.19	0.44	235
	Y_{FE}	in phase	7,000	16,000	0.19	0.64	336
		out of phase	8,000	12,000	0.25	0.53	318
Imbalance mass (330 mg), u_{DE} = 7.56 μm and u_{FE} = 14.0 μm							
Drive end	X_{DE}	in phase	7,900	8,000	0.45	0.11	122
		out of phase	6,500	7,000	0.31	0.26	236
	Y_{DE}	in phase	7,500	10,000	0.41	0.47	485
		out of phase	5,500	6,000	0.22	0.28	215
Free End	X_{FE}	in phase	8,500	9,000	0.29	0.23	149
		out of phase	7,500	9,000	0.22	0.39	221
	Y_{FE}	in phase	7,500	8,000	0.22	0.25	139
		out of phase	6,000	6,100	0.14	0.13	58

X: vertical, *Y*: horizontal. ω_n and ω_{cr} are determined from synchronous rotor responses with uncertainty of ±500 rpm. Rotor masses supported on the drive end and free end bearings are 0.66 kg and 0.36 kg, respectively.

APPENDIX C. Normalized amplitude and phase angle of synchronous response at drive end bearing, vertical plane for increasing side pressures: Original GFBs.
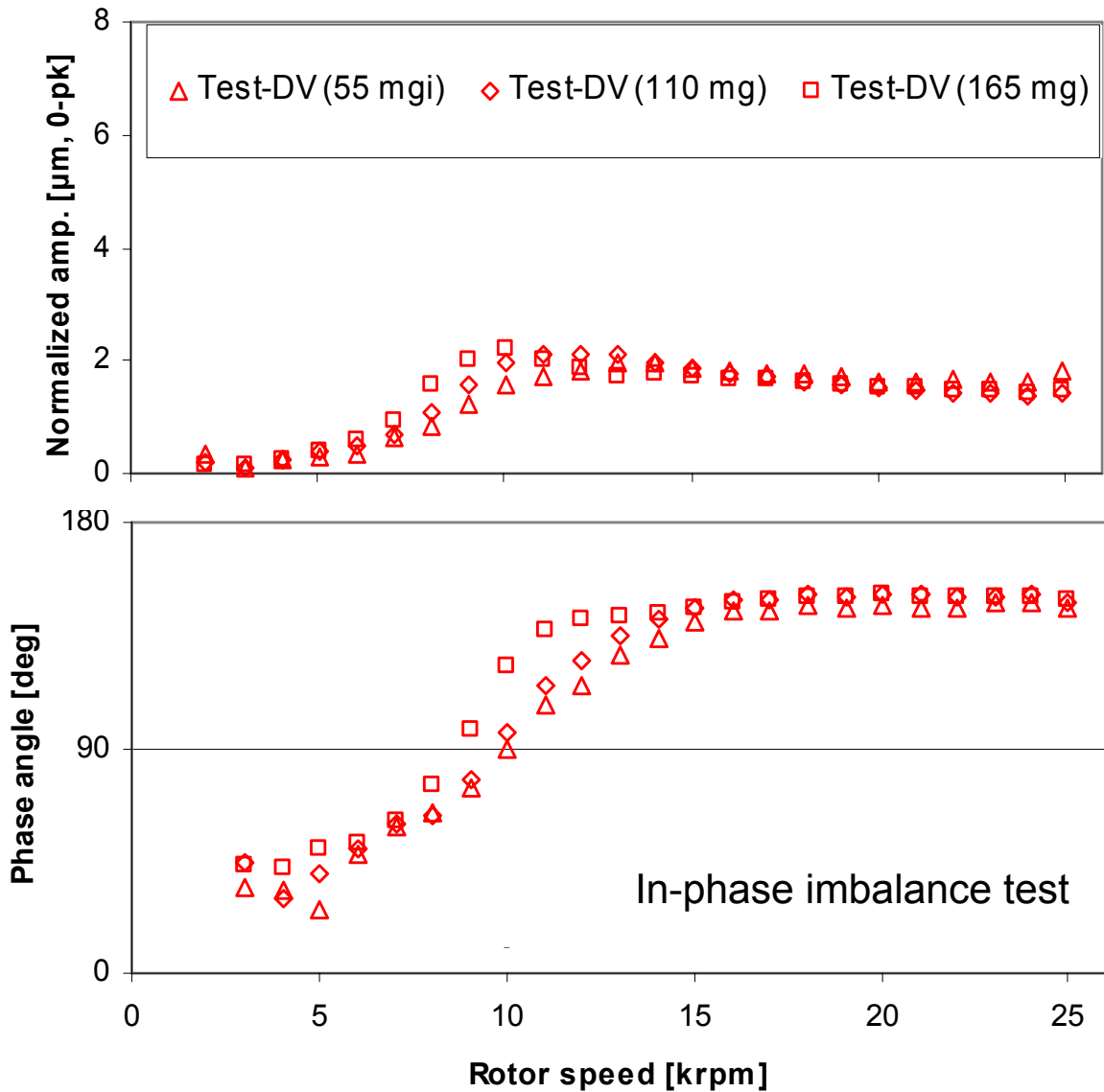

Figure C1a. Normalized amplitude and phase angle of synchronous response for side gauge pressure at 1.4 bar (20 psig). In-phase imbalance masses of 55mg, 110mg, and 165mg. Measurement at drive end bearing, vertical plane with baseline subtraction. Original GFBs.
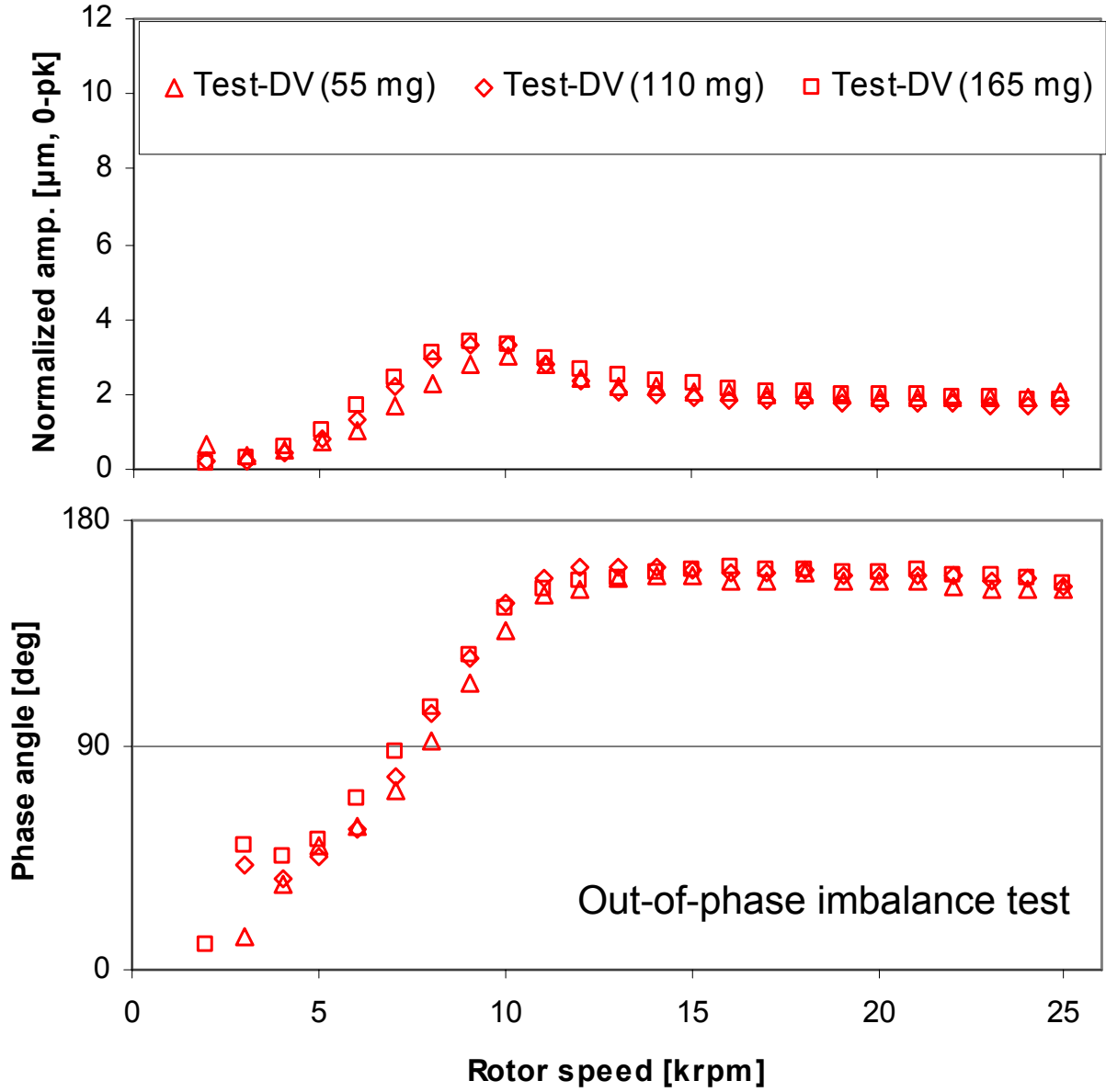
Figure C1b. Normalized amplitude and phase angle of synchronous response for side gauge pressure at 1.4 bar (20 psig). Out-of-phase imbalance masses of 55mg, 110mg, and 165mg. Measurement at drive end bearing, vertical plane with baseline subtraction. Original GFBs.
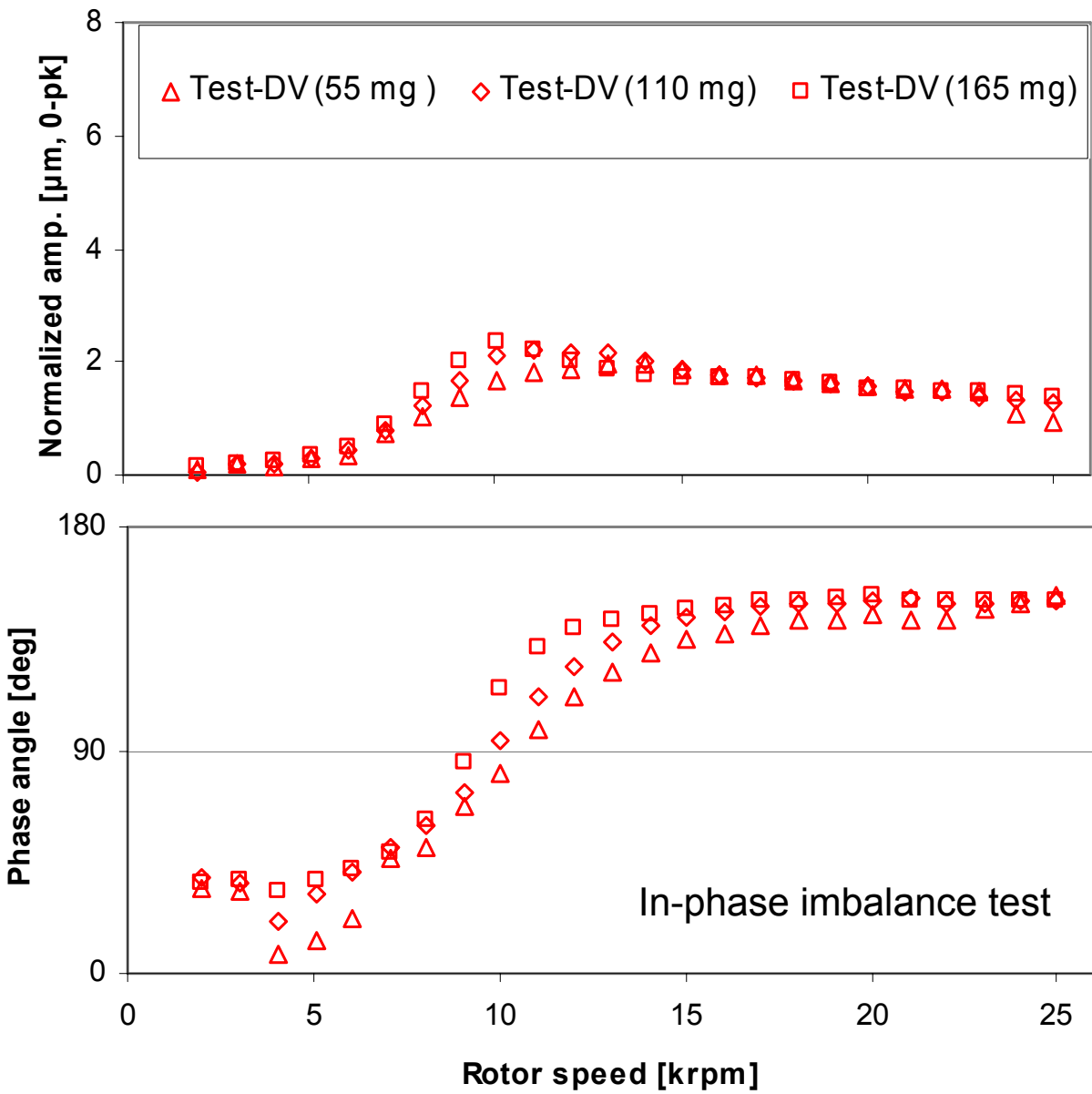
Figure C2a. Normalized amplitude and phase angle of synchronous response for side gauge pressure at 2.8 bar (40 psig). In-phase imbalance masses of 55mg, 110mg, and 165mg. Measurement at drive end bearing, vertical plane with baseline subtraction. Original GFBs.
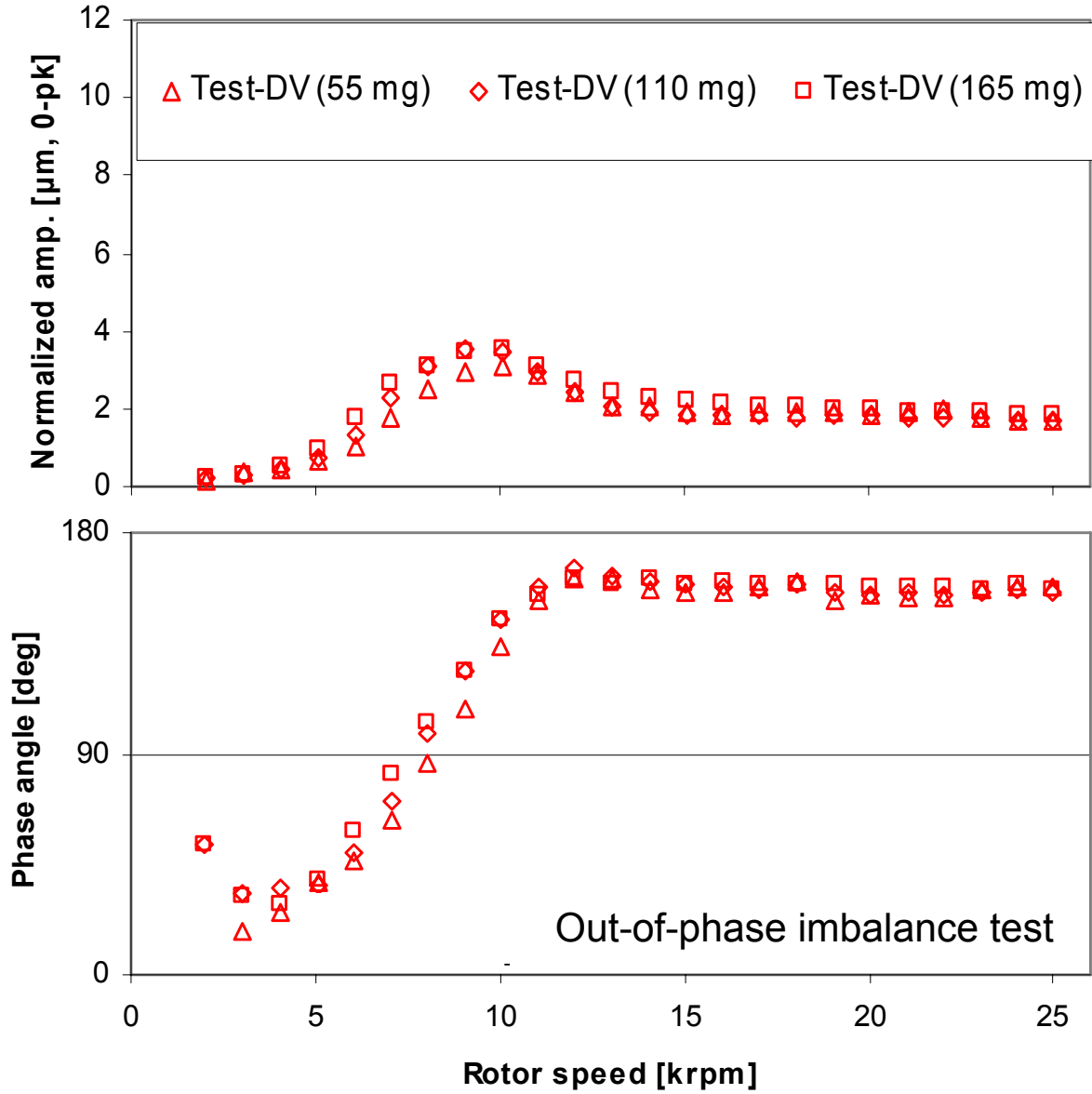
Figure C2b. Normalized amplitude and phase angle of synchronous response for side gauge pressure at 2.8 bar (40 psig). Out-of-phase imbalance masses of 55mg, 110mg, and 165mg. Measurement at drive end bearing, vertical plane with baseline subtraction. Original GFBs.

APPENDIX D. Rotor speed-up response from 10 krpm to 50 krpm for GFBs with shims. Baseline imbalance condition.

(a) Waterfall

(b) Synchronous and subsynchronous components
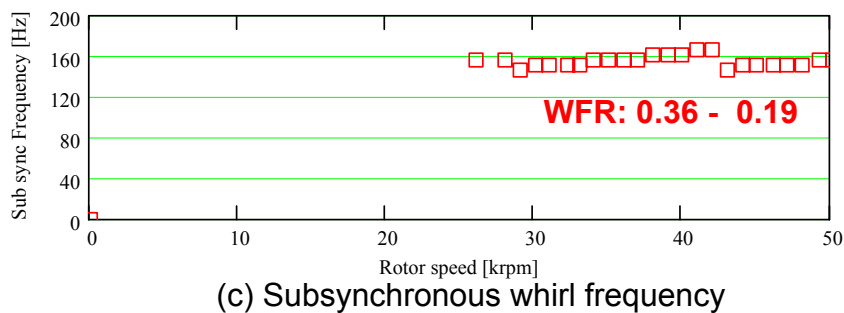

(c) Subsynchronous whirl frequency

Figure D1. Rotor speed-up response from 10 krpm to 50 krpm. Baseline imbalance condition, side air pressure of 0.34 bar (5 psig). Measurement at rotor free end, vertical plane. GFBs with shims.

(a) Waterfall

(b) Synchronous and subsynchronous components
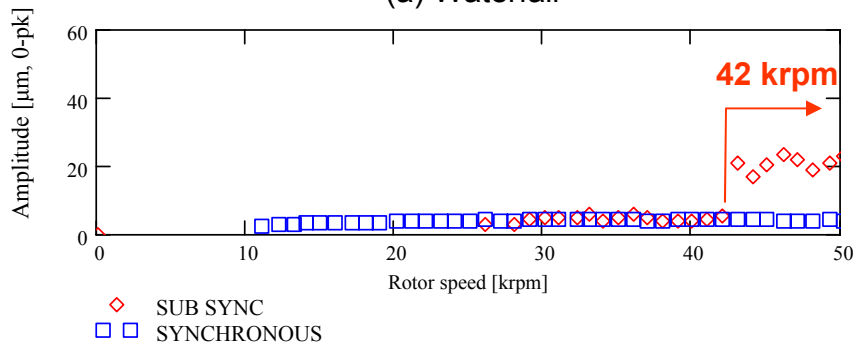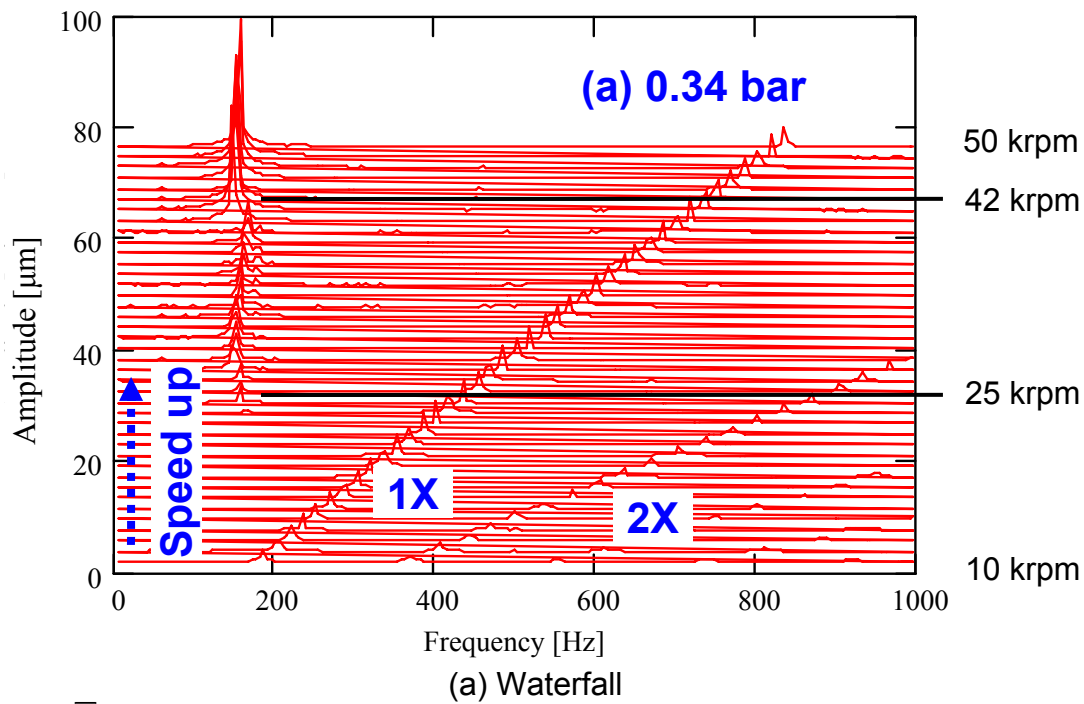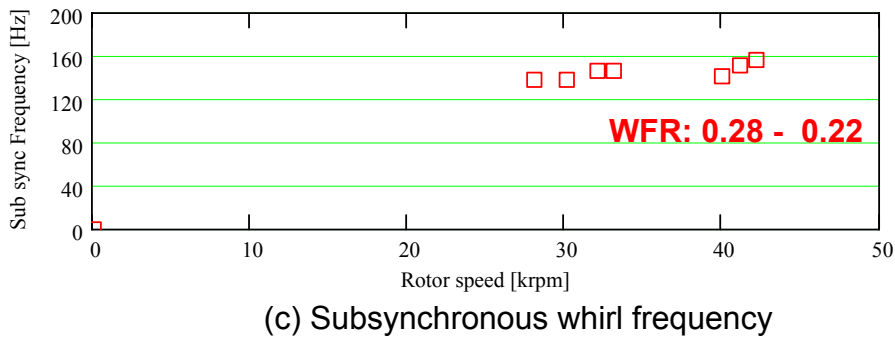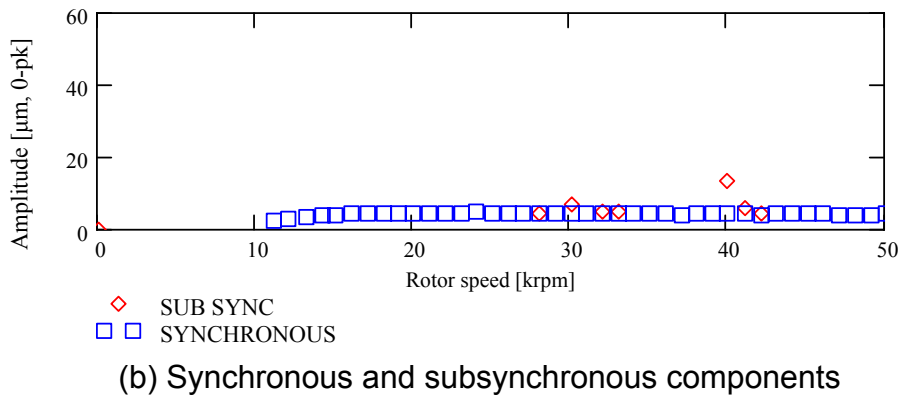
(c) Subsynchronous whirl frequency
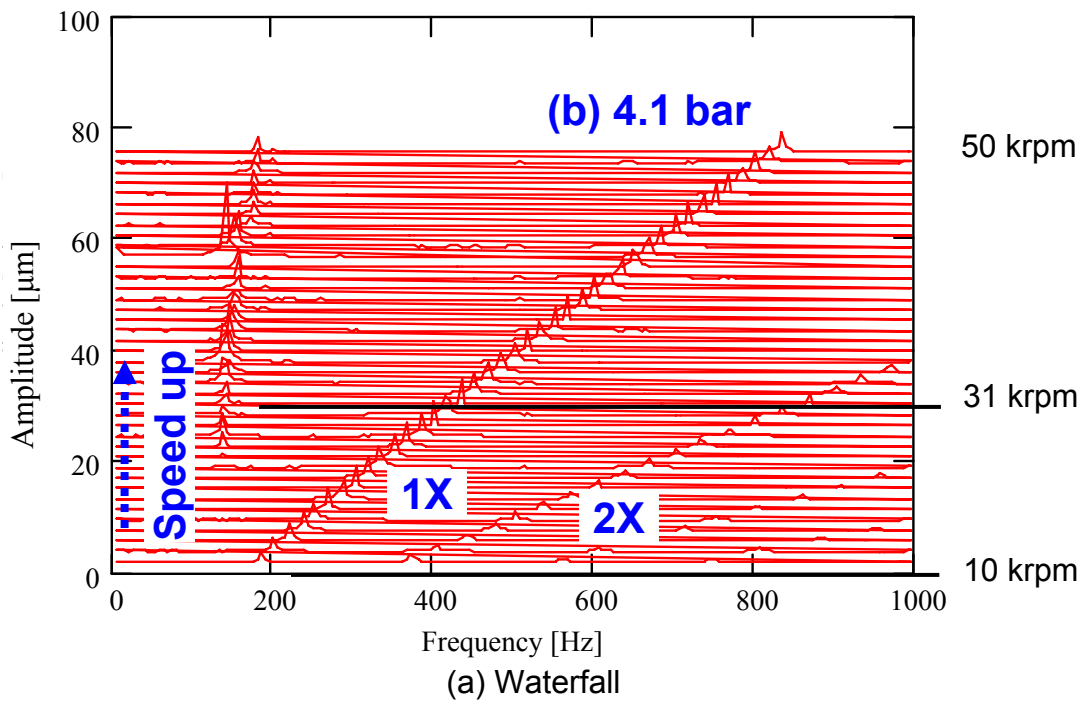
Figure D2. Rotor speed-up response from 10 krpm to 50 krpm. Baseline imbalance condition, side air pressure of 4.1 bar (60 psig). Measurement at rotor free end, vertical plane. GFBs with shims.

APPENDIX E. Normalized amplitude and phase angle of synchronous response at free end bearing, vertical plane: GFBs with shims.

Figure E1a. Normalized amplitude of synchronous response and phase angle for in-phase imbalance masses of 55mg and 110mg. Measurements at free end bearing, vertical plane with baseline subtraction. Side gauge pressure at 0.34 bar (5 psig). GFBs with shims.

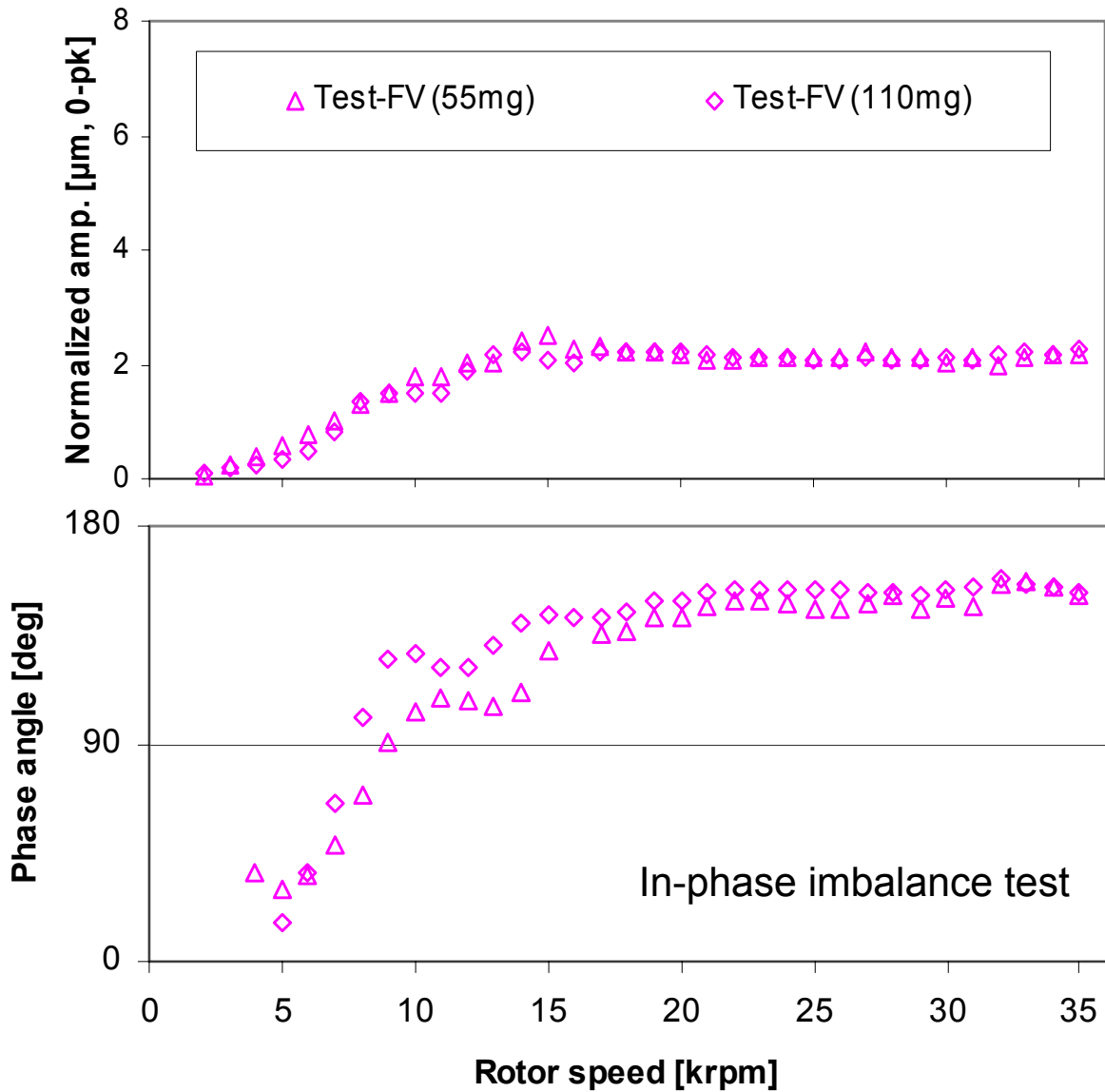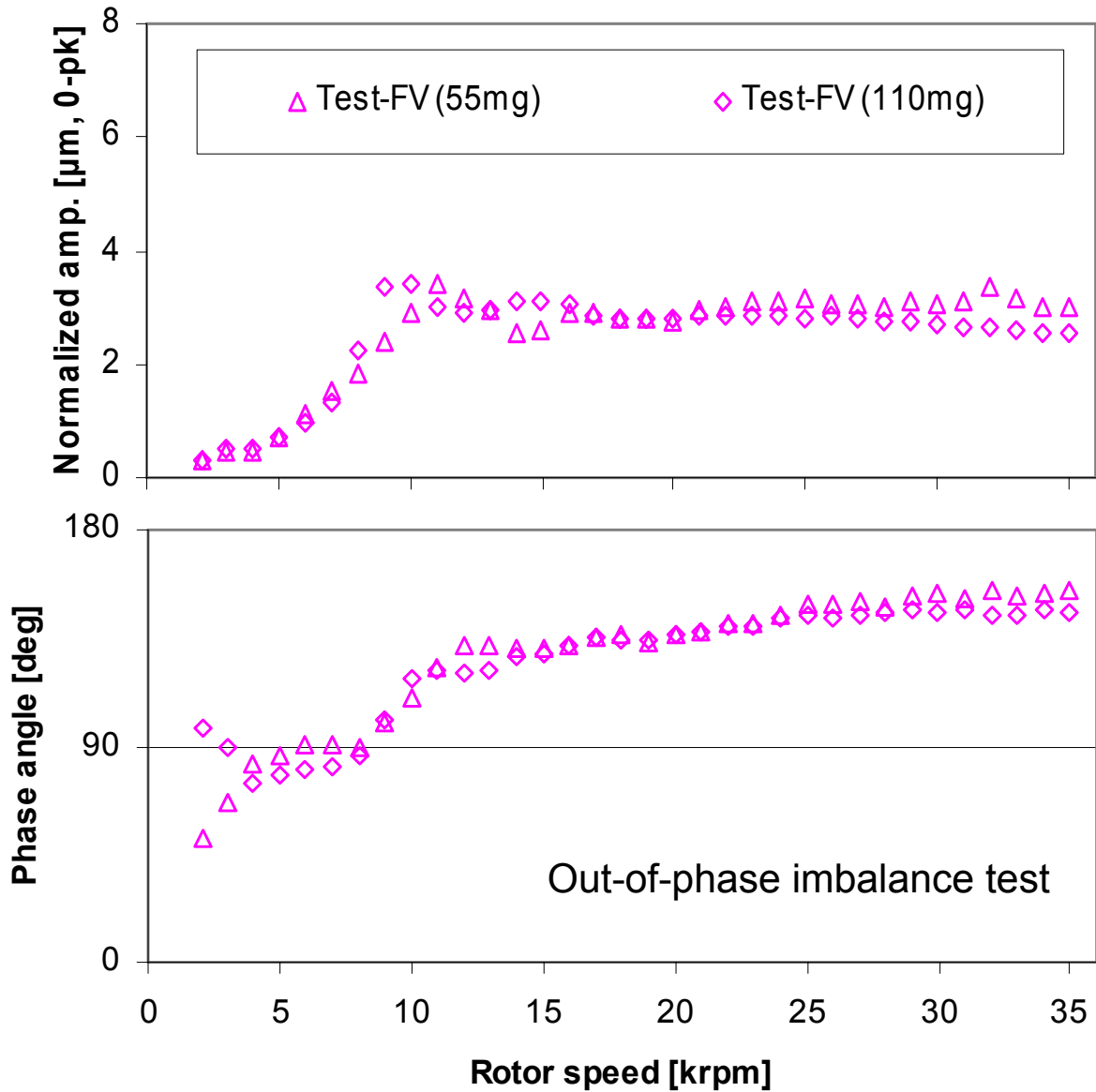**Figure E1b. Normalized amplitude of synchronous response and phase angle for out-of-phase imbalance masses of 55mg and 110mg. Measurements at free end bearing, vertical plane with baseline subtraction. Side gauge pressure at 0.34 bar (5 psig). GFBs with shims.**

APPENDIX F. Rotordynamic parameters of rotor and GFBs with shims

Table F1. Estimated rotordynamic parameters of the rotor-GFB system obtained from synchronous coastdown responses, GFB configuration with shims. Side air gauge pressure at 0.34 bar (5 psig): GFB with shims.

Location		Imbalance Condition	Natural frequency, $\omega_n \times (30/\pi)$ [rpm]	Critical Speed, $\omega_{cr} \times (30/\pi)$ [rpm]	Effective stiffness, K_{eff} [MN/m]	Damping ratio, ξ	Effective damping, C_{eff} [N-s/m]
Imbalance mass (55 mg) , u_{DE} = 1.26 μm and u_{FE} = 2.34 μm							
Drive end	X_{DE}	in phase	13,800	14,000	1.38	0.12	227
		out of phase	12,000	19,000	1.04	0.55	909
	Y_{DE}	in phase	15,500	16,000	1.74	0.18	376
		out of phase	13,500	15,000	1.32	0.31	575
Free End	X_{FE}	in phase	9,000	15,000	0.32	0.57	384
		out of phase	8,000	11,000	0.25	0.49	293
	Y_{FE}	in phase	11,000	16,000	0.48	0.51	426
		out of phase	11,500	13,000	0.52	0.33	286
Imbalance mass (110 mg) , u_{DE} = 2.52 μm and u_{FE} = 4.67 μm							
Drive end	X_{DE}	in phase	12,000	13,000	1.04	0.27	451
		out of phase	9,000	18,000	0.59	0.61	762
	Y_{DE}	in phase	14,500	14,000	1.52	-	-
		out of phase	11,500	13,000	0.96	0.33	524
Free End	X_{FE}	in phase	7,500	18,000	0.22	0.64	363
		out of phase	8,000	10,000	0.25	0.42	256
	Y_{FE}	in phase	9,800	16,000	0.38	0.56	413
		out of phase	10,800	11,000	0.46	0.13	109

X: vertical, *Y*: horizontal. ω_n and ω_{cr} are determined from synchronous rotor responses with uncertainty of ±500 rpm. Rotor masses supported on the drive end and free end bearings are 0.66 kg and 0.36 kg, respectively.

APPENDIX G. Estimation of radial clearances in original GFBs and stiffness coefficient of the flexible coupling.

A series of static load – deflection tests aids to estimate the nominal radial clearances in the test GFBs. Figure G1 shows the schematic view of the test setup. The test rotor is mounted on a lathe, and the drive and free end GFBs are installed on the rotor at the same axial locations as in the rotordynamic test rig. A strain gauge type load cell is mounted on the lathe table and connected to the test GFBs through an adapter. Moving the lathe table forward and backward provides compression and tension forces, respectively, to the GFBs through the adapter. The load cell and an eddy current displacement sensor measure the applied static load and the bearing displacement, respectively. The orientation of the spot weld in the test GFB is 45 º away from the load direction.

With the test GFB resting on the test rotor, moving forward (1) the lathe table incrementally increases the static load on the bearing at 45 º from the spot weld, and then moving it backward (2) decreases the load. When the recorded load becomes zero, moving the table backward (2) incrementally increases the load on the bearing at -135 º from the spot weld, and then moving it forward (1) reduces the load. This procedure is repeated twice for both the drive and free end GFBs, and the static load and bearing displacement are all recorded. Table G1 provides lathe table moving directions for each loading and unloading tests. Figure G2 illustrates the recorded bearing displacement versus static load.
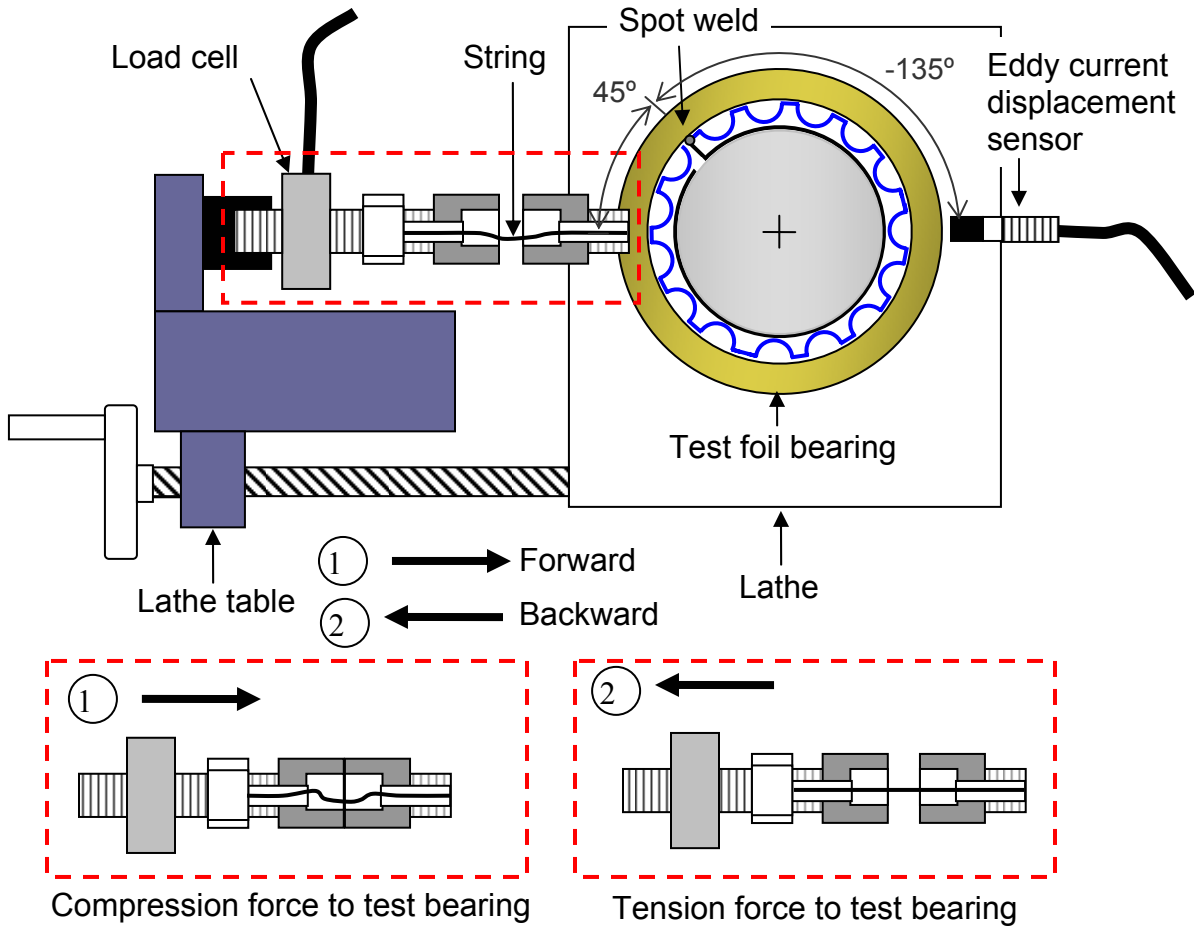
Figure G1. Schematic view of a test setup for GFB load-deflection tests

**Table G1. Load – deflection test procedure and test numbers**

Test No.	Table moving direction	Loading / Unloading
Test 1	① →	Loading
Test 2	② ←	Unloading
Test 3	② ←	Loading
Test 4	① →	Unloading
Test 5	① →	Loading
Test 6	② ←	Unloading
Test 7	② ←	Loading
Test 8	① →	Unloading

The test results in Fig. G2 show a typical nonlinear load – deflection relationship for consecutive tests conducted with the (a) drive and (b) free end GFBs. The overall behavior of the load – deflection curves seems consistent for each GFB, showing a typical hysteresis loop.

Dividing small changes in static load by the corresponding changes in bearing displacements determines the static stiffness coefficient of the foil bearings. Figure G3 shows the estimated stiffness coefficient versus bearing displacement for tests 2 – 3 and 4 – 5 with the drive and free end GFBs. Irregularly distributed preloads in the GFBs (due to fabrication inaccuracy) may cause very low stiffness around the origin in bearing displacement. Thus, the nominal radial clearances are determined as 40 μm and 70 μm for the drive (c_{DE}) and free (c_{FE}) end GFBs, respectively. With the higher bearing displacements, the support bumps start to react to the applied loads and the stiffness coefficients increase. Note that the zoomed photo of the drive end GFB in Fig. G4 evidences vividly the loose contact of the top foil to the bump strip layers due to fabrication inaccuracy in the radii of curvature of the formed top foil and bump strip layer.
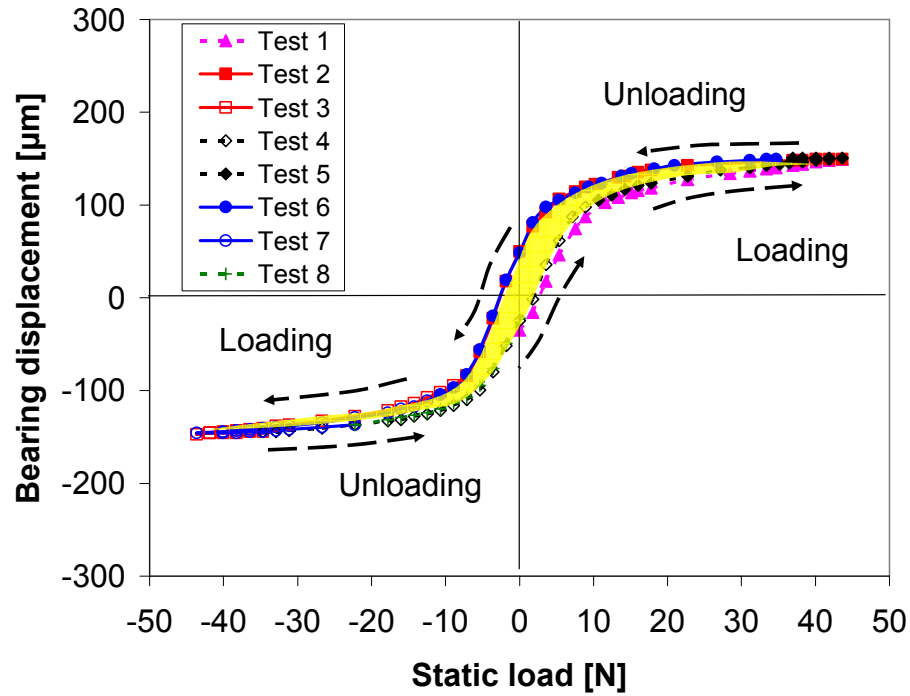
(a) Drive end foil bearing
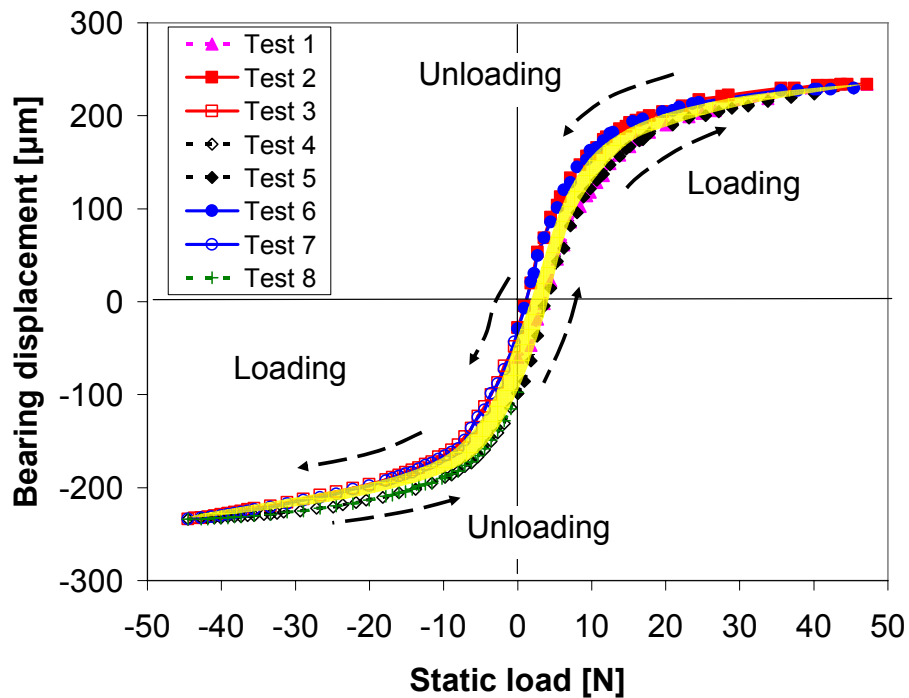
(b) Free end foil bearing

Figure G2. Measured bearing displacement versus static load for eight consecutive loading - unloading tests. (a) Drive end foil bearing, (b) Free end foil bearing. Original GFBs.
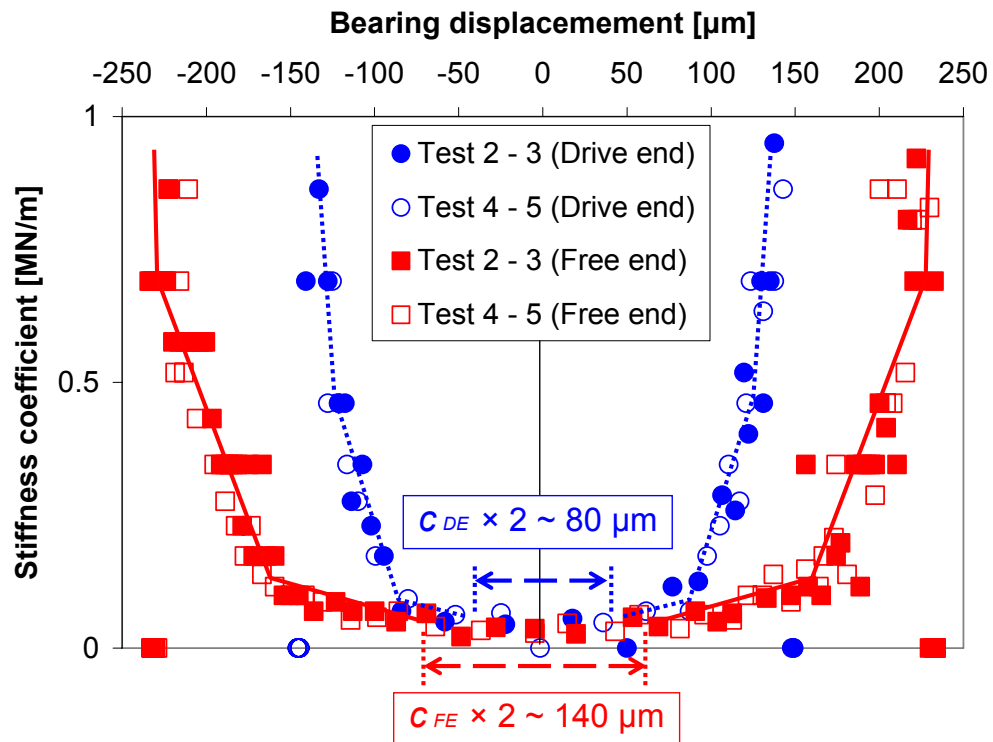
Figure G3. Stiffness coefficient versus bearing displacement for tests 2 – 3 and 4 - 5. Drive and free end bearings. Original GFBs.
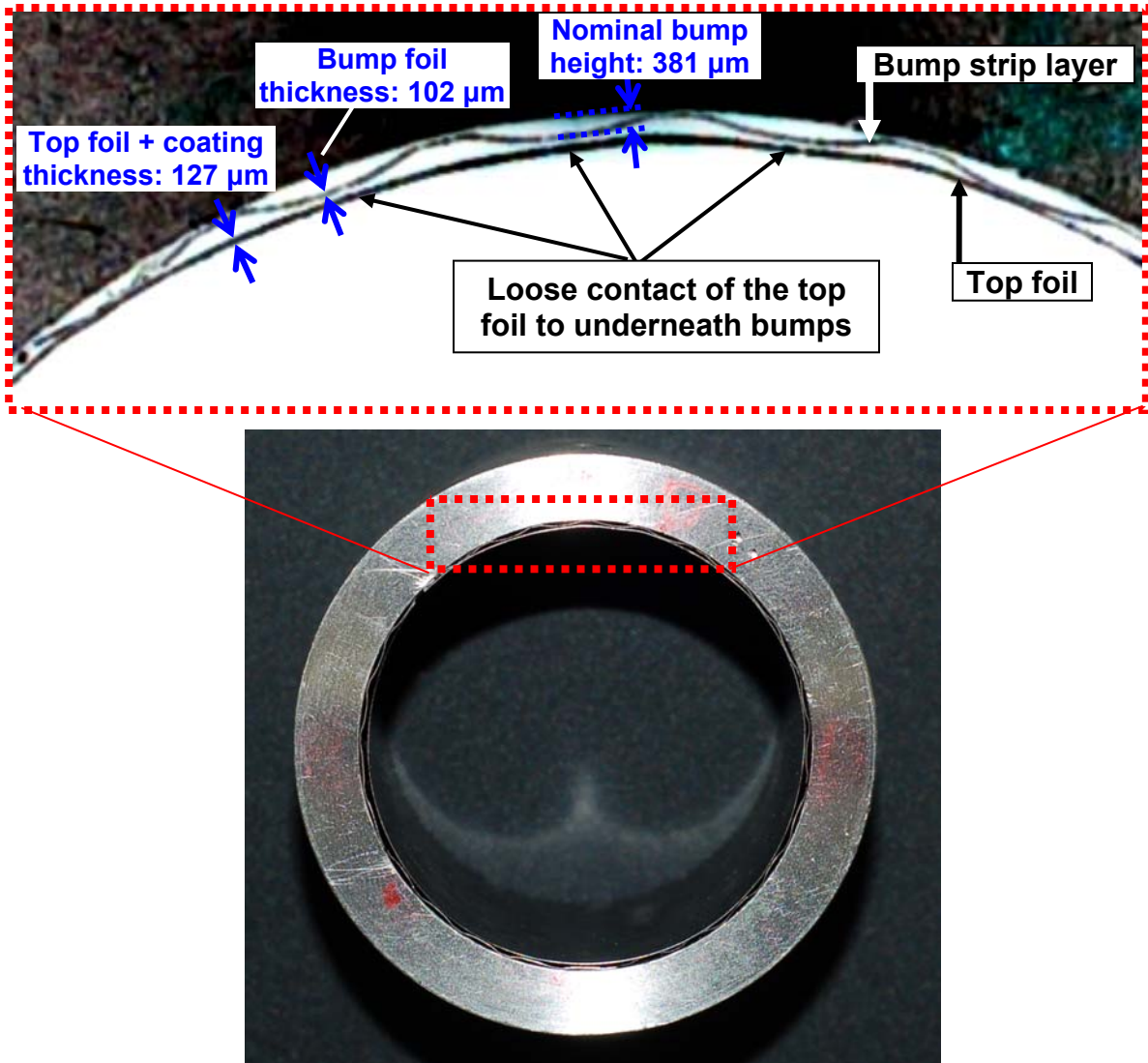
Figure G4. Zoomed photo of test (drive end) GFB. Nominal dimensions of top foil thickness, bump foil thickness, and bump height denoted. Original GFBs.

A static load – deflection test on the flexible coupling aids to estimate its stiffness coefficient. Figures G5 and G6 present the measured coupling displacement versus static load for two different dead weight locations and the estimated stiffness coefficient versus coupling displacement, respectively. Note that the averaged coupling stiffness coefficient of ~1000 N/m is an order of magnitude smaller than the least GFB stiffness coefficient (within the nominal clearance, c_{FE}) of ~ 30,000 N/m.
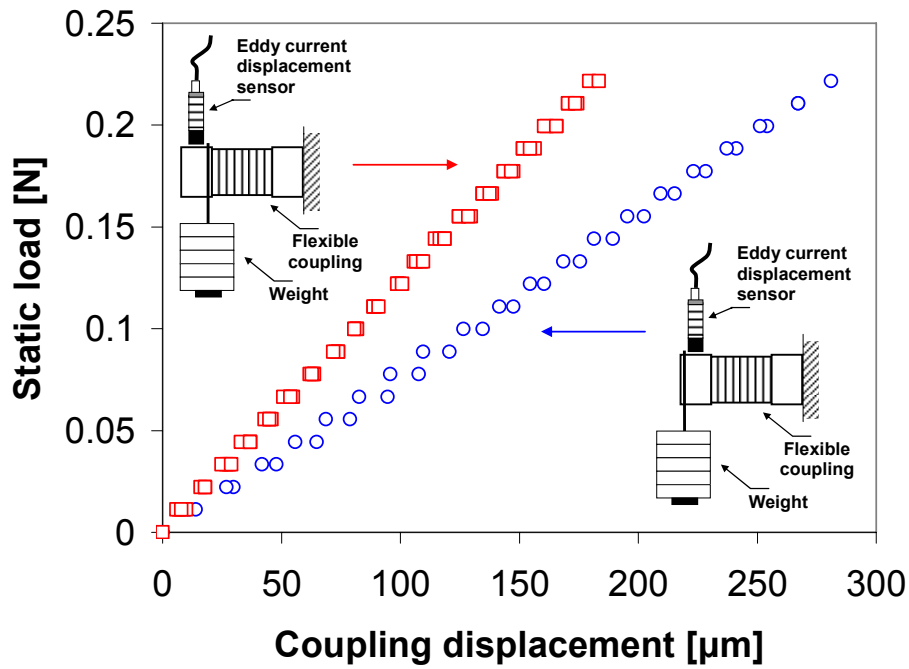
Figure G5. Measured coupling displacement versus static load for two different dead weight locations.
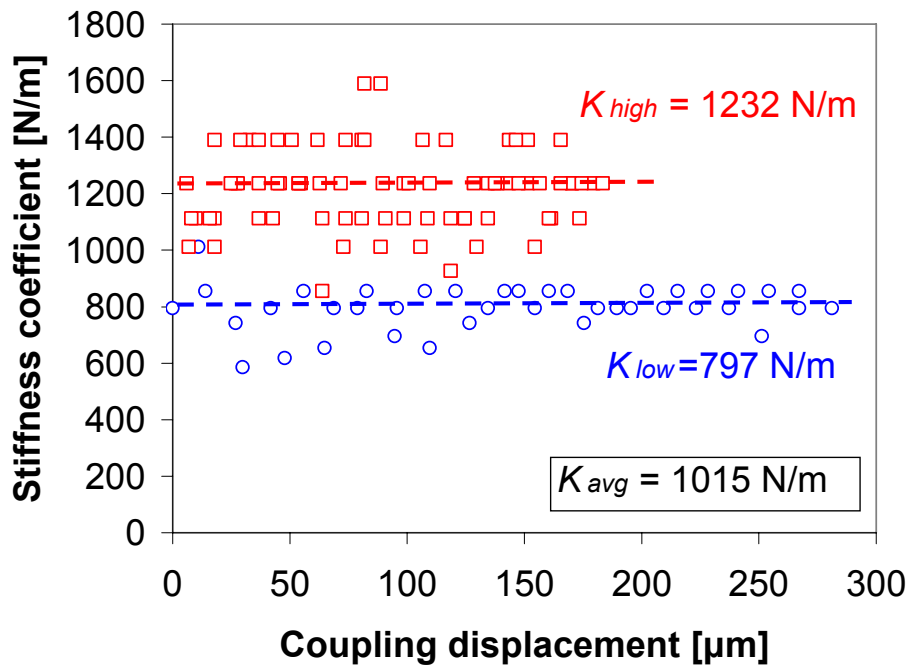

Figure G6. Estimated coupling stiffness coefficient versus coupling displacement for two different dead weight locations.